LRRK2 regulates dendritic spine dynamics through interaction with post-synaptic actin cytoskeleton

Giulia Tombesi[1], Chuyu Chen[2], Giulia Favetta[1], Nicoletta Plotegher[1,6], Martina Sevegnani[3], Antonella Marte[4], Ilaria Battisti[5], Laura Civiero[1,6,7], Franco Onofri[4], Giovanni Piccoli[3], Giorgio Arrigoni[5], Claudia Manzoni[8], Loukia Parisiadou[2] and Elisa Greggio[1,6,*]

[1]Department of Biology, University of Padova, Italy
[2]Northwest University, Chicago, USA
[3]CIBIO, University of Trento, Italy
[4]Department of Biomedical Sciences, University of Genova, Italy
[5]Department of Biomedical Sciences, University of Padova, Italy
[6]Centro Studi per la Neurodegenerazione (CESNE), University of Padova, Italy
[7]IRCCS San Camillo Hospital, Venice, Italy
[8]School of Pharmacy, UCL, UK

*Correspondence to: elisa.greggio@unipd.it, Department of Biology, University of Padova, via Ugo Bassi 58/B, 35131, Italy

Running title: LRRK2 regulates spine dynamics through actin cytoskeleton

Keywords: LRRK2, actin cytoskeleton, drebrin, BDNF, postsynapse, Parkinson's disease

Abstract

Dendritic spines, small protrusions of the dendrites, constitute the postsynaptic compartment of excitatory synapses. Filamentous actin is the major cytoskeletal constituent of dendritic spines, whose dynamic nature allows them to plastically remodel their shape and volume in response to stimuli. Notably, dendritic spine abnormalities are linked to a number of neurological and neurodegenerative disorders. Here, we show that the Parkinson disease (PD)-associated kinase LRRK2 participates in spine remodeling processing by binding a panel of actin-related proteins enriched in postsynaptic compartments. Phosphorylation of LRRK2 Ser935, which controls LRRK2 subcellular localization, rapidly increases upon brain-derived neurotrophic factor (BDNF) stimulation of differentiated SH-SY5Y cells and primary mouse neurons. Affinity-purification coupled with mass spectrometry (AP-MS/MS) analysis revealed that LRRK2 interactome is significantly reshaped upon BDNF stimulation, with an interconnected network of actin cytoskeleton-associated proteins increasing their binding to LRRK2. Accordingly, Lrrk2 knockout primary neurons exhibit impaired response to BDNF-induced spinogenesis and TrkB signaling. *In vivo*, one-month old *Lrrk2* knockout mice exhibit defects in spine maturation, a phenotype that disappears with age. Finally, by comparing the phosphoproteomes of Lrrk2 wild-type versus Lrrk2 G2019S PD mutant synaptosomes, we found that the differentially phosphorylated proteins are enriched in categories related to postsynaptic structural organization. Taken together, our study discloses a critical function of LRRK2 in shaping dendritic spine morphology during development and defines a mechanistic role of the kinase in postsynaptic actin-cytoskeletal dynamics.

Introduction

Synapses constitute a key element in the nervous system that ensures the execution of body functions and higher associative processes such as cognition, memory, behavior and personality. In the great majority of neurons the total area of the dendritic tree is increased by the presence of small and specialized protrusions known as dendritic spines that represent the postsynaptic element of most excitatory synapses[1–3]. Dendritic spines typically possess a bulbous head attached to the dendritic shaft by a narrow neck[4] and according to detailed anatomical studies, they are classified into distinct morphological categories[5,6]. It is widely accepted that spines with larger heads originate stronger synaptic contacts and, accordingly, they are defined as mature protrusions. Indeed, the head size is proportional to the area of the post synaptic density, to the number of postsynaptic neurotransmitter receptors and also the amount of presynaptic docked vesicles[3].

Dendritic spines exhibit the ability to change their morphology, number, density and motility over periods ranging from minutes to days and months, representing highly dynamic and plastic elements[7]. The formation and loss of dendritic spines as well as their morphological plasticity is driven by actin cytoskeleton rearrangements[8]. Actin is a major constituent of dendritic spines and able to rapidly polymerize and depolymerize, constituting a very efficient tool for coupling synaptic activity to dendritic spines structural adaptation[9]. These modifications occur throughout the entire lifespan in response to environmental cues, a process known as synaptic plasticity. Synaptic plasticity is crucial during the development and maturation of the organism, but also in the process of learning and memory and in the recovery after brain damage. Thus, neuronal communication requires functional and also plastic neuronal circuits and any impairment in this system can harm the correct information transfer, leading to pathology.

Robust literature indicates synaptic damage and connectome dysfunction as an early pathological event proceeding neurodegeneration and clinical symptoms in multiple neurodegenerative disorders, including Parkinson's disease (PD)[10–14]. PD is a age-related motor disorder for which no cure is available. The motor symptoms typically manifest as a consequence of the progressive loss of the dopaminergic neurons of the Substantia Nigra pars compacta (SNpc) projecting to the striatum[15]. The degeneration of the nigrostriatal projections precedes the loss of the dopaminergic cell body in the SNpc and synaptic failure may be the triggering cause of axonal deterioration [13,16]. Pre and postsynaptic alterations were reported also in PD animal models[13]. For example, PD associates with an evident striatal spine loss, that appears to be correlated with the degree of dopamine denervation and that is prevalently due to glutamate excitotoxicity in striatal neurons [17,18].

Accumulating evidence indicate that more than half of causative genes and risk factors for PD function at the synapse. Mutations in LRRK2 gene represent the most common cause of autosomal dominant late onset familial PD and variations around LRRK2 locus increase lifetime risk for PD[19]. Pathogenic mutations are clustered into the enzymatic core of LRRK2 protein, composed by a Roc/GTPase and kinase domains, bridged by a COR scaffold [20–22]. The

most frequent mutation (G2019S) located in the kinase domain results in a protein with a gain of kinase activity, associated with increased cellular toxicity [20]. Previous data from our team and other laboratories suggest that LRRK2 sits at the crossroads between cytoskeletal dynamics and vesicular traffic, through interaction with a host of cytoskeletal and vesicle-associated proteins and phosphorylation of a subset of Rab GTPases [23,24]. LRRK2 subcellular localization is dynamically controlled by phosphorylation/dephosphorylation of a cluster of N-terminal serine residues (e.g. Ser935 and Ser910), which determines 14-3-3 protein binding and LRRK2 subcellular localization[25]. This activity is particularly important in a specialized compartment such as the synapse as it provides the scaffold for the assembly of local signalling and the achievement of the main synaptic functions[23]. In the presynaptic site LRRK2 has been shown to regulate synaptic vesicles cycling through interaction and phosphorylation of a panel of pre-synaptic proteins[26], such as NSF and synapsin I [27,28]. Interestingly, recent literature support a role for LRRK2 in dendritic spine compartment, where it influences receptor traffic [29] and spine morphology and functionality in developing brains [30–32]**.** LRRK2 is highly expressed in spiny projecting neurons (SPNs) of the dorsal striatum[33,34], the postsynaptic element of the nigrostriatal pathway rich in dendritic spines.

Here, starting from the observation that brain derived neurotrophic factor (BDNF) stimulates LRRK2 Ser935 phosphorylation in neurons, we used unbiased protein-protein interaction (PPI) studies and phosphoproteomic investigations to disclose a novel function of LRRK2 in regulating actin-dependent postsynaptic structural dynamics.

Results

BDNF treatment rapidly increases LRRK2 phosphorylation at Ser935

Phosphorylation of LRRK2 Ser935 and Ser910 is regulated by multiple kinases, including casein kinase 1 alpha (CK1a), IKKs and protein kinase A (PKA)[35–37], and serves as a scaffold for 14-3-3 protein binding and LRRK2 subcellular localization[25,38]. In immune cells, extracellular signals such as Toll-like receptor 4 (TLR4) agonists stimulate this phosphorylation to positively modulate immune-related responses[35,39]. In contrast, the extracellular signals that orchestrate Ser935 phosphorylation in neurons are unknown. By binding to receptor tyrosine kinases, cognate neurotrophic factors plastically shape neuronal activity[40]. Brain-derived neurotrophic factor (BDNF) is particularly important to modulate cortico-striatal neurotransmission[41], a circuitry relevant for PD where LRRK2 expression is higher compared to other brain regions [42,43]. To address whether LRRK2 Ser935 phosphorylation is stimulated by BDNF, we prepared primary mouse cortical neurons from C57BL/6J wild-type mice and stimulated them with 100 ng/ml of BDNF at days in vitro 14 (DIV14) when synapses are fully functional (**Figure 1a**) and LRRK2 expression is detectable[44]. Western blot analysis revealed a rapid (5 mins) and transient increase of Ser935 phosphorylation after BDNF treatment (**Figure 1b** and **1c**). Of interest, BDNF failed to stimulate Ser935 phosphorylation when neurons were pretreated with the LRRK2 inhibitor MLi-2, indicating that either LRRK2 kinase activity

controls the upstream kinases activated by BDNF or that the binding with MLi-2, a type I inhibitor, locks the kinase in a conformation that favors dephosphorylation/hinders phosphorylation[45].

To gain mechanistic insights into the effects of BDNF stimulation on LRRK2 function, we established a more accessible experimental model. To this end, we differentiated neuroblastoma SH-SY5Y with 10 µM retinoic acid (RA) treatment for 6 days[46] and measured BDNF response by monitoring Tropomyosin receptor kinase B (TrkB) levels and phosphorylation of AKT and ERK1/2, two major downstream effector pathways of BDNF/TrkB signaling (**Figure 1d**)[47]. Expression of TrkB is undetectable in undifferentiated SH-SY5Y cells, whereas RA-differentiation boosts TrkB expression (**Figure 1e**). Accordingly, differentiated SH-SY5Y cells respond to 100 ng/ml BDNF stimulation, as evidenced by increased phosphorylation of ERK1/2 and AKT (**Figure 1f**). Strikingly, BDNF treatment stimulates Ser935 phosphorylation of endogenous LRRK2 with a phosphorylation kinetics overlapping with that observed in primary neurons (**Figure 1h**). These findings support RA-differentiated SH-SY5Y as a valuable model to investigate a novel BDNF-LRRK2 pathway.

BDNF promotes LRRK2 interaction with actin cytoskeleton components enriched at the postsynapse.

To clarify the implications of BDNF-mediated Ser935 phosphorylation on LRRK2 neuronal function, we used affinity purification coupled with mass spectrometry (AP-MS/MS). As the yields of endogenous LRRK2 purification were insufficient for AP-MS/MS analysis, we generated polyclonal SH-SY5Y cells stably expressing GFP-LRRK2 wild-type or GFP control. First, we confirmed that RA-differentiated SH-SY5Y GFP-LRRK2 cells were able to respond to BDNF treatment by increasing LRRK2 Ser935 phosphorylation (**Figure S1**). Then we used GFP-trap purification to isolate GFP or GFP-LRRK2 from RA-differentiated cells unstimulated or stimulated with BDNF for 15 mins prior to MS analysis. The unstimulated LRRK2 interactome (GFP-LRRK2 vs. GFP) is large (207 significant hits) and consistent with previous computational analysis of LRRK2 PPIs [48,49]. In particular, we confirmed interactions with known LRRK2 binders including 14-3-3 proteins, cytoskeletal proteins and protein translation factors (**Figure 2a**). Since BDNF is synaptically released and influences pre- and post-synaptic mechanisms, we used SynGO[50] to identify synaptic LRRK2 interactors (red-colored in **Figure 2a**). About one-third (35%) of LRRK2 PPI are SynGO annotated genes; among them, 33% are presynaptic proteins and 66% are post-synaptic proteins (**Figure 2b**). The most significant enriched categories were pre- and post-synaptic ribosome and post-synaptic actin cytoskeleton (**Figure 2b**).

We next compared unstimulated vs. BDNF-stimulated LRRK2 interactome. As shown in **figure 2c**, 15 minutes of BDNF stimulation reshapes LRRK2 PPI, with a group of interactors increasing binding with LRRK2 (blue dots) and another group decreasing binding (orange dots). The inclusion criteria were either p value < 0.05 and fold change (FC) > 1 or FC > 2 independently from the p-value. In this way, we increased the discovery power for gene ontology analysis. SynGO gene ontology revealed that 10 out of 19 hits with increased binding after BDNF

(BDNF(+)) and 21 out of 50 hits with decreased binding (BDNF(-)) are synaptic proteins (**Figure 2c** inset). Among synaptic interactors, the BDNF(+) binders are enriched in actin-cytoskeleton-related GO:BP categories while the BDNF(-) binders are enriched in protein translation GO:BP categories (**Figure 2d**). Furthermore, 80% of synaptic BDNF(+) LRRK2 binders (DBN1, ARPC2, ACTR2, ACTR3, CFL1, CALD1, ACTN1, FLNA) and 62% of synaptic BDNF(-) binders (RPS2, RPS4X, RPS7, RPS9, RPS11, RPS13, RPS15A, RPL13, RPL23, RPL26, RPL27A, TUFM, EEF1A2, PCBP1) form functional and physical interaction networks (**Figure 3e**).

To validate these findings, we performed western blot analysis on the AP samples analyzed by MS. We selected drebrin, encoded by *DBN1*, because it sits at the center of the BDNF(+) network (**Figure 2e**). As predicted, BDNF treatment increases LRRK2:drebrin interaction by ~2 fold (**Figure 2f** and **2g**). In DIV14 primary neurons, drebrin colocalizes with PSD95, a postsynaptic marker (**Figure 2h**), confirming previous observations[51]. We conclude that BDNF stimulation engages LRRK2 into actin cytoskeleton dynamics through physical association with actin-related proteins. This stimulus-dependent function may be relevant at the postsynaptic site (**Figure 2b** and **2h**). Our findings also suggest that a pool of LRRK2 binds protein translation factors under unstimulated conditions and translocates to the actin-cytoskeleton upon BDNF-TrkB signaling.

BDNF-induced spinogenesis is impaired in *Lrrk2* knockout neurons.

Since BDNF induces dendritic spine formation, maturation and structural plasticity[52,53] and BDNF(+) LRRK2 interactors are actin-related proteins enriched at the postsynapse (**Figure 2**), we set out to investigate whether loss of LRRK2 interferes with BDNF-induced spine morphogenesis. Primary cortical neurons were transfected with GFP at DIV4 and treated with BDNF for 24 h at DIV13 (**Figure 3a**). Consistent with previous findings[54,55], BDNF treatment significantly increased the density of dendritic spines in WT cultures ($p < 0.001$). In contrast, BDNF failed to induce spinogenesis in *Lrrk2* knockout (KO) neurons. Without exogenous BDNF, spine density was comparable in WT and KO neurons (**Figure 3b-c**). These data support a crucial role for LRRK2 in spine morphogenesis in response to BDNF.

To corroborate these observations, we evaluated the downstream signaling components of the BDNF-TrkB pathway (**Figure 1d**). *Lrrk2* WT and KO primary cortical neurons at DIV14 were stimulated with BDNF at different timepoints (0, 5, 15, 30, 60 mins). As expected, *Lrrk2* WT neurons responded to BDNF by rapidly increasing Akt and Erk1/2 phosphorylation. In contrast, KO cells exhibited a significantly reduced phosphorylation of Akt and Erk1 (**Figure 3d-e**). Of note, 90 mins of Lrrk2 inhibition (MLi-2) prior to BDNF stimulation did not prevent phosphorylation of Akt and Erk1/2, suggesting that LRRK2 participates in BDNF-induced phosphorylation of Akt and Erk1/2 independently from its kinase activity but dependently from its ability to be phosphorylated at Ser935 (**Figure 3d** and **Figure 1b-c**).

Dendritic spine maturation is delayed in *Lrrk2* knockout mice.

Based on the *in vitro* results indicating that BDNF stimulates the recruitment of LRRK2 through Ser935 phosphorylation and binding to actin-cytoskeleton to promote spinogenesis, we next investigated whether loss of *Lrrk2 in vivo* results in dendritic spine defects. During development, dendritic spines are highly dynamic, with a rate of extension and retraction that allows proper and accurate synapse formation and neuronal circuit assembly[7]. By the adulthood, dendritic spines formation, motility, and pruning decrease reaching a relatively stable number of protrusions[56]. Since spines dynamics vary according to the stage of brain development, we performed a longitudinal analysis of young (1 month-old), adult (4 month-old) and aged (18 month-old) *Lrrk2* WT and KO mice in order to capture any age-dependent defect (**Figure 4a**). We focused on the dorsal striatum, a region highly enriched in SPNs that receives excitatory afferents from the cortex and dopaminergic modulation from the SNpc. This region is relevant in the prodromal stages of PD neurodegeneration[57] and expresses high levels of LRRK2[42,58] and several studies showed a key role of LRRK2 in shaping the structure and function of excitatory synapses in the striatum[30,31,59,60]. We evaluated the number and morphology of dendritic spines using Golgi-Cox staining (**Figure 4b**). The total number of protrusions varied across ages, but there were no differences between the two genotypes (**Figure 4c**). Instead, the width and the length of the protrusions were reduced in 1 month-old Lrrk2 KO striata with respect to WT. Specifically, the average neck height was 15% shorter and the average head width was 27% smaller, meaning that spines are smaller in *Lrrk2* KO brains. No differences were observed at 4 and 18 months of age (**Figure 4c**). We then classified the morphology of spines into four categories: filopodia and thin protrusions (immature spines) and mushroom and branched protrusions (mature spines). As shown in **figure 4d**, 1 month-old *Lrrk2* KO animals exhibit a reduced number of filopodia and an increased quantity of thin protrusions, suggesting that loss of Lrrk2 may favor this transition. Instead, the proportion of mature spines (mushroom and branched) remained unaltered. No differences were observed in older mice (**Figure 4d**).

Since the overall width/height of *Lrrk2* KO protrusions is reduced (**Figure 4c**), we next analyzed the postsynaptic ultrastructure using electron microscopy. To increase the experimental power, we used a separate group of animals. We measured the postsynaptic density (PSD) length as it directly correlates with the amount of postsynaptic receptors and signaling proteins, thus providing an indication of the synaptic strength (**Figure 4e**). PSD is significantly shorter in 1 month-old *Lrrk2* KO animals compared to WT ($p < 0.001$), while no differences in PSD length are observed in 18 month-old KO mice (**Figure 4f**). Taken all these data together, we conclude that subtle postsynaptic maturation defects are present in the striatum of post-natal *Lrrk2* KO mice.

To establish whether loss of *Lrrk2* in young mice causes a reduction in dendritic spines size by influencing BDNF-TrkB expression, we measured *Bdnf* and *TrkB* transcripts, as well as *Psd95* and *Shank3*, two major postsynaptic scaffolds. Neither *Bdnf* nor *TrkB* expression is altered in the striatum, cortex or midbrain of 1-month old Lrrk2 KO as compared to WT mice (**Figure 4g**), supporting a mechanism whereby LRRK2 is influenced by BDNF signaling, but the absence

of LRRK2 does not affect *Bdnf* or *TrkB* expression. Instead - and as expected - *Psd95* and *Shank3* expression is lower in *Lrrk2* KO mice and, interestingly, the effect is not limited to the striatum but is also found in the cortex and midbrain. Taken together, our results indicate that LRRK2 influences dendritic spines maturation in the developing brain.

Phosphoproteome of Lrrk2^{G2019S} synaptosomes is enriched in postsynaptic structure organization SynGO terms.

Our data so far indicate that LRRK2 influences the shape of postsynaptic structures by engaging in complex formation with actin-cytoskeleton elements. We then asked whether the kinase activity of LRRK2 may also play a role in these morphogenetic processes. We purified synaptosomes from WT and hyperactive Lrrk2^{G2019S} knockin (KI) mice and performed phosphopeptide enrichment and MS analysis (**Figure 5a**). Synaptosomal preparations are highly enriched in pre- and postsynaptic components[30]. We identified 2957 phosphopeptides common between WT and Lrrk2^{G2019S} synaptosomes. Among them, 343 phosphopeptides showed a significant decrease or increased phosphorylation in Lrrk2^{G2019S} with respect to WT (**Figure 5b**). The LRRK2 kinase substrates Rabs are not present in the list of significant phosphopeptides, likely due to the low stoichiometry and/or abundance. Next, by overlapping the list of proteins containing at least 1 significant phosphopeptide (267 proteins) with the list of AP-MS interactors identified in SH-SY5Y cells (207 proteins) (**Figure 2a-b**), we found 5 proteins in common (CEP170, HSP90AB1, MAP1B, TUBA1A and DBN1) highlighted with colored dots in the volcano plot (**Figure 5b**). One hundred thousand random lists containing 207 proteins each (to mimic the AP-MS list) and overlapping them with the 267 significant genes in phosphoproteomic dataset results in a distribution of overlaps peaking around 2, indicating that 5 overlaps is not a random event. Four (CEP170, HSP90AB1, MAP1B and TUBA1A) were previously reported LRRK2 interactors[25,61–64]. Strikingly, DBN1, encoding for drebrin, is a key BDNF(+) LRRK2 interactor sitting in the center of the network (**Figure 2e**) and validated by secondary assays (**Figure 2f-g**). Drebrin is an actin-binding protein enriched at dendritic spines[65], whose binding with actin is regulated by Cdk5-mediated phosphorylation at Ser142[66]. In our dataset however, the phosphorylation of this site is not affected by Lrrk2^{G2019S} activity, instead we observed a significant reduction of a peptide containing two phosphorylated residues (S385 and S387 in mouse and S337 and S339 in human drebrin), previously reported by multiple high throughput studies (https://www.phosphosite.org/homeAction). The lower phosphorylation of this drebrin peptide in Lrrk2^{G2019S} implies that the effect is indirect. Possible kinases phosphorylating these sites are Cdk5 and PKA (NetPhos 3.1 Server[67,68]), providing clues on regulatory mechanisms underlying LRRK2:drebrin binding.

Next, we performed GO analysis of differentially phosphorylated proteins using SynGO. Biological processes (BP) significantly enriched include synaptic vesicle cycle/exocytosis and postsynaptic structural organization (**Figure 5c**). Enrichment by cellular components (CC) similarly indicates synaptic vesicles and postsynaptic density/cytoskeleton as enriched terms (**Figure 4d**). This analysis confirms the established role of LRRK2 as a crucial regulator of

synaptic vesicles cycle[26] and further support a previously underestimated function of LRRK2 in regulating postsynaptic structural plasticity.

Discussion

Understanding the early events that lead to synaptic dysfunction in PD is crucial to design effective therapeutic approaches. Previous work from our laboratories and other groups have shown that the PD-associated kinase LRRK2 regulates important synaptic processes. At the presynapse, LRRK2 controls synaptic vesicles cycle through association with its WD40 domain [69–72] and phosphorylation of a panel of presynaptic proteins, including N-ethylmaleimide sensitive fusion (NSF)[27], synapsin I[28], auxilin[73], synaptojanin[74] and Endophylin A[75]. At the postsynapse, LRRK2 plays key roles in shaping the function of excitatory synapses in the striatum [30,31,59,60,76]. However, the mechanisms underlying LRRK2 postsynaptic activity remain unresolved. In the present study we provide multiple lines of evidence that LRRK2 shapes dendritic spines morphology in response to BDNF neurotrophic stimulation, which promotes relocalization of LRRK2 to the actin-cytoskeleton in a phosphorylation-dependent manner.

There are several novel findings in our study. First, we identify BDNF as an extracellular stimulus increasing LRRK2 Ser935 phosphorylation in neurons. The phosphorylation kinetics are fast and transient, and Lrrk2 KO neurons display reduced Akt and Erk downstream pathways activation, all consistent with an early signaling event in the cascade. Using an unbiased PPI approach, we found that LRRK2 associates with an highly interconnected network of actin-binding proteins after rapid (15 mins) BDNF stimulation. Moreover, loss of *Lrrk2* results in impaired BDNF-induced spinogenesis *in vitro* and delayed spine maturation *in vivo*, pointing to a mechanism whereby BDNF-mediated Ser935 phosphorylation engages LRRK2 into a macromolecular complex required to coordinate actin dynamics during postsynaptic structural plasticity. Accordingly, BDNF is key to reorganize the actin cytoskeleton during long term potentiation (LTP) through the action of Rho GTPases Rac1 and Cdc42[77]. LRRK2 was previously reported to interact with Rac1[78,79] and with other actin-related proteins[80]. Here we demonstrate that LRRK2 association with actin cytoskeleton in dendritic spines is stimulus-dependent. We validated the BDNF-dependency of the interaction between LRRK2 and drebrin, an actin binding protein that promotes stable F-actin formation in dendritic spines [51]. We found that drebrin phosphorylation at Ser337/Ser339 is significantly lower in synaptosomes from hyperactive Lrrk2 G2019S mice, further strengthening the physiological relevance of this interaction. Loss of drebrin results in delayed synaptogenesis and inhibition of postsynaptic PSD95 accumulation, suggesting a key role in spine maturation[51,81,82]. During LTP, Ca^{2+} entry through N-methyl-d-aspartate (NMDA) receptors causes drebrin exodus from the spine compartment to allow actin monomers entrance and polymerization to increase the size of the cytoskeleton[83]. We postulate that LRRK2 may favor drebrin exodus at the shaft of the dendrite during plasticity processes. Actin remodeling during spine enlargement is also coordinated by the ARP2/3 complex, which is activated by binding to WAVE family proteins downstream of active Rac1[84]. Strikingly, we found that BDNF

stimulates LRRK2 interaction with three out of seven subunits of the ARP2/3 complex (ACTR2, ACTR3 and ARPC2) and LRRK2 was reported to interact with WAVE proteins[85]. Altogether these findings, in agreement with our earlier study[32], highlight a crucial role for LRRK2 in actin-based dendritic spine remodeling. Future studies should be directed at clarifying the precise molecular dynamics and kinetics of these processes.

Another interesting aspect disclosed here is that loss of LRRK2 phenotypically manifests during development, while spine defects maturation normalize with age. This is not surprising considering that the homologous kinase LRRK1 may compensate for LRRK2 deficiency, as suggested by the overt neurodegeneration observed in double *Lrrk1/Lrrk2* KO mice but absent in the single KO[86,87] and the redundant but not overlapping pattern of expression of the two kinases[88]. Indeed, striatal Lrrk2 expression in the rodent brain increases up to postnatal week 4[32,58,88,89], while Lrrk1 transcript in this region is relatively stable during development[58].

Our phosphoproteomic analysis of WT vs. G2019S striatal synaptosomes revealed that LRRK2 kinase activity plays two major and distinct functions at pre- and postsynaptic compartments: regulation of synaptic vesicle cycle and organization of postsynaptic cytoskeleton and density. Accordingly, ultrastructural and expression analyses showed reduced postsynaptic density in 1 month-old *Lrrk2* KO mice. There is a tight connection between postsynaptic density organization/expansion and actin cytoskeleton. Interactions of the F-actin binding protein Abp1 with members of the Shank family, such as Shank3, serve as anchoring points for the dynamics of postsynaptic actin cytoskeleton[90]. Reduced expression of Shank3 and Psd95 in 1 month-old Lrrk2 mice further support these connections.

Several lines of evidence indicate that genetic, biochemical and cellular alterations of BDNF/TrkB signaling are linked to PD. At striatal synapses, BDNF/TrkB signaling enhances both dopamine and glutamate release and ERK1/2 activation[91,92]. BDNF is required for the establishment of the proper number and for the survival of dopaminergic neurons in the SNpc [93,94], and presynaptic dopamine release in the striatum is enhanced by BDNF[41]. BDNF levels are lower in peripheral tissues, brain, and blood of sporadic PD patients[95]. Moreover, the V66M polymorphism modifies the risk of sporadic and mutant LRRK2-associated PD[96,97]. Decreased BDNF concentration in serum and brain correlates with an increased degeneration of dopaminergic neurons in PD[98] and with loss of striatal DA transporter (DAT) in patients with striatal dopaminergic neurodegeneration[99]. Thus, robust literature support deregulation of striatal BDNF signaling in PD. Future studies should be directed at investigating possible deregulations of BDNF signaling in G2019S mutant mice.

At the onset of PD, loss of dopaminergic axonal terminals largely exceeds loss of cell bodies [14], implying that early synapse deterioration may be the trigger of axonal degeneration and, ultimately, neuronal death[100]. In contrast to neuronal loss, which is irreversible, disease-associated synaptic dysfunctions could be rescued through the growth of new terminals and/or dendritic spines[13]. Thus, focusing on early, prodromal dysfunction in PD appears key

to design effective therapeutic and preventive strategies, and our study uncovered LRRK2 as a promising disease modifying target of early-stage PD.

Materials and methods

Mouse strains

C57Bl/6J Lrrk2 knock-out (KO) and G2019S-Lrrk2 knock-in mice were provided by Dr. Heather Melrose (Mayo Clinics, Florida, USA). Housing and handling of mice were done in compliance with national guidelines. All animal procedures were approved by the Ethical Committee of the University of Padova and the Italian Ministry of Health (license 1041/2016-PR and 105/2019) and followed the guidelines approved by the Northwestern University Animal Care and Use Committee. Approximately equal numbers of males and females were used for every experiment.

Cell cultures

SH-SY5Y cell line maintenance, differentiation and treatments

Human neuroblastoma-derived SH-SY5Y cells (naïve, overexpressing GFP or LRRK2 tagged with GFP) were cultured in a complete medium composed of a 1:1 mixture of Dulbecco's Modified Eagle's Medium (DMEM, ThermoFisher Scientific) and Ham's F-12 Nutrient Mixture (F12, ThermoFisher Scientific), supplemented with 10% v/v Fetal Bovine Serum (FBS, ThermoFisher Scientific) and 1% Penicillin/Streptomycin solution (PS, ThermoFisher Scientific). Cells were maintained in complete medium at 37°C in a humified atmosphere with 5% CO2.

To promote N-type (neuronal-like cells) cell differentiation, cells were plated in DMEM/F12 containing 1% PS, 1% FBS and 10µM of all-trans-retinoic acid (RA, Sigma-Aldrich). Cells were subsequently incubated at 37°C in 5% CO2. At regular intervals of 48 hours, RA was newly provided to the differentiating cells. Cells were incubated again at 37°C in 5% CO2 and the differentiation process was carried on until differentiation day 6, when cells were subjected to the treatments.

On differentiation day 6, the differentiation media was completely removed from each dish and replaced with DMEM/F12 added with only 1% PS. Human neuroblastoma-derived SH-SY5Y cells were serum-starved for 5 hours at 37°C in 5% CO2. Then, the inhibition of LRRK2 kinase activity was achieved by pre-treating cells with 0.5 µM MLi-2 (ab254528, Abcam) for 1.5 hour. Hence, in the same serum-free medium, cells were stimulated for different time periods (5, 15, 30 and 60 minutes) with BDNF (100ng/mL, 50240-MNAS, Sino Biological) in the presence or absence of the LRRK2 inhibitor.

Primary mouse cortical neuron preparation, transfection and treatments

Primary cortical neurons from Lrrk2 WT and KO C57BL/6J mice were derived from postnatal mouse (P0) exploiting the Papain Dissociation System (Worthington Biochemical

Corporation). The brain was removed from the skull and, once isolated in dissection medium (10mM HEPES pH 7.3, D-glucose 0.1%, sodium pyruvate 0.11mg/ml in Hanks' Balanced Salt Solution) cortices were snipped into smaller pieces and transferred in Papain solution (Papain and DNase solution in Earle's Balanced Salt Solution) where they were further triturated 10 times. Then, the solution was incubated for 40 minutes at 37°C and was mixed by inversion every 10 minutes. Subsequently, cells were triturated 10 times and spun down in a swinging-bucket rotor for 5 minutes at 200g. The supernatant was discarded and 3mL of Stop solution [DNase solution and Trypsin inhibitor solution (15,5mg/ml) in Earle's Balanced Salt Solution] was added to the pellet: after triturating 3 times, the tubes were incubated for 10 minutes at room temperature to allow the bigger pieces of tissue to precipitate. Then, the supernatant was gently pipetted drop-by-drop upon 5mL of 10/10 solution (10 µg/ml Trypsin inhibitor and 10 µg/ml BSA in Earle's Balanced Salt Solution) and spun down for 10 minutes at 100g. After discarding the supernatant, the pellet was resuspended in about 5mL of Neurobasal A (Life Technologies) medium supplemented with 2% v/v B27 Supplements (Life Technologies), 0.5 mM L- glutamine (Life Technologies), 100 U/mL penicillin, and 100 µg/mL streptomycin (Life Technologies) and cells were diluted to 1:10 in 0.4% Trypan blue to be counted. Neurons were plated at 1000-1500 cells/mm2 onto 6-well plates or at 200 cell/mm2 on 12mm glass coverslips in 24-well plates and maintained in culture for 14 days prior to the treatments. After 7 days, 50% of the Neurobasal medium was removed and replaced with fresh one.
One reach the fourteenth day in vitro, Lrrk2 WT and KO mature neurons cultured in the 6-well plates for WB analysis were subjected to BDNF (100ng/mL) and Mli2 (0.5µM) treatments for 5, 30, 60 and 180 minutes in Neurobasal completed medium. Four days after the seeding, Lrrk2 WT and KO primary neurons plated in 24-well plates were transiently transfected using Lipofectamine 2000 (Invitrogen) with a DNA(µg):Lipofectamine(µl) ratio of 1:2. A total amount of 1µg DNA was dissolved in 250µl of OPTI-MEM (Life Technologies) and the respective amount of LIPO was added to 250µl of OPTI-MEM. The solutions were mixed together after 5 minutes and incubated for 20 minutes to allow the formation of DNA/LIPO complexes. The mix was then added drop by drop to neurons, whose medium was previously changed with OPTI-MEM. After 45 minutes of incubation the transfection medium were replaced with the supplemented Neurobasal and neurons were maintained in culture for additional 9-10 days. At DIV14, neurons were treated for 24 hours with BDNF (100ng/mL) to study the spinogenesis process.

Protein purification from mammalian cells

For the purification protocol, SH-SY5Y OE-GFP and SH-SY5Y OE-hLRRK2-GFP were plated onto 100mm dishes (Sarstedt Limited) and differentiated into neuronal-like cells for 6 days. On differentiation day 6, SH-SY5Y OE-hLRRK2-GFP cells were treated with recombinant BDNF (100ng/mL) or with an equal volume of Cell Culture Water Pyrogen free for 15 minutes, while SH-SY5Y OE-GFP cells were left untreated. Once the treatment medium was removed, cells were washed with PBS and, then, solubilized in 500µL of Lysis Buffer (20mM Tris-HCl pH 7.5, 150mM NaCl, 1mM EDTA, 1% Tween 20, 2.5mM sodium pyrophosphate, 1mM β-

glycerophosphate, 1mM sodium orthovanadate) containing 1% protease inhibitor cocktail. After clearing of the lysates containing GPF-tagged protein by centrifugation at 20000g for 30 minutes at 4°C, the supernatants were incubated overnight with an appropriate volume of GFP-Trap Agarose resin (ChromoTek, Planegg-Martinsried, Germany) overnight at 4°C in rotation. Resins were subsequently washed twice with different Washing Buffers (WB) supplemented with Tween 20 (WB1: 20mM Tris-HCl pH 7.5, 500mM NaCl, 1% Tween 20; WB2: 20mM Tris-HCl pH 7.5, 300mM NaCl, 0.5% Tween 20; WB3: 20mM Tris-HCl pH 7.5, 150mM NaCl, 0.5% Tween 20; WB4: 20mM Tris-HCl pH 7.5, 150mM NaCl, 0.1% Tween 20; WB5: 20mM Tris-HCl pH 7.5, 150mM NaCl, 0.02% Tween 20). Centrifugation steps (7500g x 1 minute) were performed between washes to pellet the resin. Proteins were eluted in sample buffer 2X and then resolved in SDS-PAGE. Acrylamide gels containing samples from SH-SY5Y OE-GFP and SH-SY5Y hLRRK2-GFP cells were stained with Colloidal Coomassie Brilliant Blue [0.25% Brilliant Blue R-250 (Sigma-Aldrich), 40% ethanol, 10% acetic acid in milli-Q water] for at least 1 hour and then destained with a destaining solution (10% isopropanol, 10% acetic acid in milli-Q water). Eventually, the gel was preserved in 10% acetic acid in agitation to remove the background color and visualize proteins. Finally, gel band was excised and assessed by mass spectrometry (MS).

Cells and tissues lysis and western blot analysis

For Western Blot analysis mammalian cells and mouse brain tissues were harvested in appropriate volume of RIPA Lysis Buffer (20mM pH 7.5 Tris-HCl, 150mM NaCl, 1mM EDTA, 1mM EGTA, 1% NP40, 1% sodium deoxycholate, 2.5mM sodium pyrophosphate, 1mM β-glycerophosphate, 1mM sodium orthovanadate) supplemented with 1% protease inhibitor cocktail (Sigma-Aldrich). More precisely, mammalian cells were lysed at the end of each treatment, after the removal of culture medium and two washes with DPBS.

The appropriate volume of each sample, containing 50µg for SH-SY5Y cells and primary neurons and 70µg for brain tissues, was denatured by diluting 4X Sample Buffer [200mM Tris-HCl pH 6.8, 8% SDS, 400mM DTT, 40% glycerol, q.s. Bromophenol Blue (Sigma-Aldrich)] to a final 1X concentration. For the AP-MS experiments, proteins were resolved on 8% Tris polyacrylamide homemade gels in SDS/Tris-glycine running buffer, while in the other cases ExpressPlus precast 4-20% gels (GenScript Biotech Corporation) in MOPS running buffer were exploited. Also, Precision Plus Protein Standard Dual Color (Bio-Rad) molecular weight marker was loaded in a separate lane of each gel. Resolved proteins were transferred to polyvinylidenedifluoride (PVDF, Bio-Rad) membranes using semidry Bio-Rad transfer machine (Trans-Blot Turbo Transfer System, Bio-Rad). The nonspecific binding sites were subsequently blocked incubating membranes with 5% non-fat dry milk diluted in 0.1% Tween-20 Tris-buffered saline (TBS-T) for 1 hour at room temperature under agitation. PVDF membranes were subsequently incubated over-night at 4°C with primary antibodies in 5% non-fat dry milk in TBS-T or in 5% BSA in TBS-T. Membranes were then washed three times in TBS-T at room temperature to remove the excess of primary antibody and subsequently incubated for 1 hour at room temperature with horseradish peroxidase (HRP)-conjugated α-mouse or α-

rabbit IgG. After three more washes in TBS-T, proteins were visualized using chemiluminescence (Immobilon ECL western HRP substrate, Millipore). Densitometric analysis was carried out using the Image J software. The antibodies used for WB are as follows: rabbit α-LRRK2 (MJFF2 c41-2, ab133474, Abcam, 1:300); rabbit α-phospho-Ser935 LRRK2 (ab133450, Abcam, 1:300); mouse α-phospho-Ser473-AKT (sc-293125, Santa Cruz Biotechnology, 1:500); rabbit α-AKT (9272S, Cell Signaling Technology, 1:1000); rabbit α-phospho [(Thr202/Tyr204, Thr185/Tyr187)-ERK1/2 (12-302, Millipore, 1:1500); rabbit α-ERK1/2 (4695, Cell Signaling Technology, 1:1000); mouse α-GAPDH (CSB-MA000195, 1:5000); mouse α-βIII tubulin (T8578, Sigma-Aldrich, 1:40000); mouse α-DREBRIN (MA1-20377, Thermo-Fisher, 1:500); α-Flag M2-HRP (A8592, Sigma-Aldrich, 1:5000); α-mouse IgG-HRP (A9044, Sigma-Aldrich, 1:80000); α-rabbit IgG-HRP (A9169, Sigma-Aldrich, 1:16000).

LC-MS/MS and data analysis

Three biological replicates were processed for the proteomics experiments. Gel slices were cut into small pieces and subjected to reduction with dithiothreitol (DTT 10 mM in 50 mM NH4HCO3, for 1 h at 56 °C), alkylation with iodoacetamide (55 mM in 50 mM NH4HCO3, for 45 min at RT and in the dark), and in-gel digestion with sequencing grade modified trypsin (Promega, 12.5 ng/µL in 50 mM NH4HCO3). Samples were analyzed with a LTQ-Orbitrap XL mass spectrometer (Thermo Fisher Scientific) coupled to a HPLC UltiMate 3000 (Dionex – Thermo Fisher Scientific) through a nanospray interface. Peptides were separated at a flow rate of 250 nL/min using an 11-cm-long capillary column (PicoFrit, 75-µm ID, 15-µm tip, New Objective) packed in house with C18 material (Aeris Peptide 3.6 µm XB C18; Phenomenex). A linear gradient of acetonitrile/0.1% formic acid from 3 to 40% was used for peptide separation and the instrument operated in a data dependent acquisition mode with a Top4 method (one full MS scan at 60,000 resolution in the Orbitrap, followed by the acquisition in the linear ion trap of the MS/MS spectra of the four most intense ions). Two technical replicates were acquired for each biological replicate. Raw data files were analyzed using MaxQuant and Andromeda software package (Tyanova, S., Temu, T., and Cox, J., The MaxQuant computational platform for mass spectrometry-based shotgun proteomics, Nat Protocols, 2016, 11, pp 2301–2319) and searched against the human section of the UniProt database (version September 2020, 75093 entries) concatenated with a database of common contaminants found in proteomic experiments. Trypsin was selected as digesting enzyme with up to two missed cleavages allowed, carbamidomethylation of cysteine residues was set as a fixed modification and methionine oxidation as a variable modification. A search against a randomized database was used to assess the false discovery rate (FDR), and data were filtered to remove contaminants and reverse sequences and keep into account only proteins identified with at least two peptides and a FDR ≤ 0.01, both at peptide and protein level.

Intensity values were retrieved for 350 proteins. A single step of data QC was applied to the intensity values: proteins whose intensity value was 0.00 for both the 2 technical replicates in at least 1 of the 3 pull-down experiments performed with LRRK2-GFP were removed. This is a stringent QC step, but it was implemented to remove proteins with no triplicate data

available for the LRRK2 pull-down as this could have occurred because of genuine low levels of pull-down (values close to the limit of detection, missing not at random values) or because of technical issues with the single sample (loss/poor quality of sample, missing at random values). QC reduced the number of proteins in the analysis from 350 to 269 entries.
Intensity data were then processed according to[101]. Briefly, intensity data were log2 transformed and normalized to the median of all proteins within the same experiment. Missing data (0.00 intensity values) were considered missing not at random thus they were imputed via probabilistic minimum imputation (random values within less than 2.5 standard deviations from the distribution of intensity values per the single experiment, 0.3 max variability) [101,102].
Finally, fold change (LRRK2-GFP vs GFP and LRRK2-GFP BDNF treated vs LRRK2-GFP untreated) and associated p-value (two-tailed, paired t-test) were calculated and visualized.

Phosphoproteomics analysis

Protein processing for MS

Striata from 8 weeks mice were dissected and rapidly homogenized in four volumes of ice-cold Buffer A (0.32 M sucrose, 5 mM HEPES, pH7.4, 1 mM MgCl2, 0.5 mM CaCl2) supplemented with Halt protease and phosphatase inhibitor cocktail (Thermo Fisher Scientific) using a Teflon homogenizer (12 strokes). Homogenized brain extract was centrifuged at 1400 g for 10 min. Supernatant (S1) was saved and pellet (P1) was homogenized in buffer A with a Teflon homogenizer (five strokes). After centrifugation at 700 g for 10 min, the supernatant (S1') was pooled with S1. Pooled S1 and S1' were centrifuged at 13,800 g for 10 min to the crude synaptosomal pellet (P2). The crude synaptosomal pellet (P2) was homogenized in buffer B (0.32M sucrose, 6mM Tris, pH 8.0) supplemented with protease and phosphatase inhibitors cocktail with a Teflon homogenizer (five strokes) and was carefully loaded onto a discontinuous sucrose gradient (0.8 M/1 M/1.2 M sucrose solution in 6 mM Tris, pH 8.0) with a Pasteur pippete, followed by centrifugation in a swinging bucket rotorfor 2 h at 82,500 g. The synaptic plasma membrane fraction (SPM) in the interphase between 1 M and 1.2 M sucrose fractions was collected using a syringe and transferred to clean ultracentrifuge tubes. 6 mM Tris buffer was added to each sample to adjust the sucrose concentration from 1.2 M to 0.32 M and the samples were centrifuged in a swinging bucket rotor at 200,000 g for 30 min. The supernatant was removed and discarded. Added to the pellets the lysis solution containing 12 mM sodium deoxycholate, 12 mM sodium lauroyl sarcosinate, 10 mM TCEP, 40 mM CAA, and phosphatase inhibitor cocktail (Millipore-Sigma) in 50 mM Tris·HCl, pH 8.5, and incubated 10 min at 95°C with vigorous shaking. Sonicated the pellets several times with a sonicator probe and boiled again for 5 min. Centrifuged at 16,000 × g for 10 min to remove the debris and collected supernatant. The samples were diluted fivefold with 50 mM triethylammonium bicarbonate and analyzed by BCA to determine protein concentration. The samples were then normalized to 300ug protein in each and digested with 6ug Lys-C (Wako) for 3 h at 37°C. 6ug trypsin was added for overnight digestion at 37°C. The supernatants were collected and acidified with

trifluoroacetic acid (TFA) to a final concentration of 1% TFA. Ethyl acetate solution was added at 1:1 ratio to the samples. The mixture was vortexed for 2 min and then centrifuged at 16,000 × g for 2 min to obtain aqueous and organic phases. The organic phase (top layer) was removed, and the aqueous phase was collected, dried completely in a vacuum centrifuge, and desalted using Top-Tip C18 tips (Glygen) according to manufacturer's instructions. The samples were dried completely in a vacuum centrifuge and subjected to phosphopeptide enrichment using PolyMAC Phosphopeptide Enrichment kit (Tymora Analytical) according to manufacturer's instructions, and the eluted phosphopeptides dried completely in a vacuum centrifuge.

LC-MS/MS Analysis

The full phosphopeptide sample was dissolved in 10.5 µL of 0.05% trifluoroacetic acid with 3% (vol/vol) acetonitrile and 10 µL of each sample was injected into an Ultimate 3000 nano UHPLC system (Thermo Fisher Scientific). Peptides were captured on a 2-cm Acclaim PepMap trap column and separated on a 50-cm column packed with ReproSil Saphir 1.8 µm C18 beads (Dr. Maisch GmbH). The mobile phase buffer consisted of 0.1% formic acid in ultrapure water (buffer A) with an eluting buffer of 0.1% formic acid in 80% (vol/vol) acetonitrile (buffer B) run with a linear 90-min gradient of 6–30% buffer B at flow rate of 300 nL/min. The UHPLC was coupled online with a Q-Exactive HF-X mass spectrometer (Thermo Fisher Scientific). The mass spectrometer was operated in the data-dependent mode, in which a full-scan MS (from m/z 375 to 1,500 with the resolution of 60,000) was followed by MS/MS of the 15 most intense ions (30,000 resolution; normalized collision energy - 28%; automatic gain control target (AGC) - 2E4, maximum injection time - 200 ms; 60sec exclusion].

LC-MS Data Processing

The raw files were searched directly against the mouse database with no redundant entries, using Byonic (Protein Metrics) and Sequest search engines loaded into Proteome Discoverer 2.3 software (Thermo Fisher Scientific). MS1 precursor mass tolerance was set at 10 ppm, and MS2 tolerance was set at 20ppm. Search criteria included a static carbamidomethylation of cysteines (+57.0214 Da), and variable modifications of phosphorylation of S, T and Y residues (+79.996 Da), oxidation (+15.9949 Da) on methionine residues and acetylation (+42.011 Da) at N terminus of proteins. Search was performed with full trypsin/P digestion and allowed a maximum of two missed cleavages on the peptides analyzed from the sequence database. The false-discovery rates of proteins and peptides were set at 0.01. All protein and peptide identifications were grouped and any redundant entries were removed. Only unique peptides and unique master proteins were reported.

Label-free Quantitation Analysis

All data were quantified using the label-free quantitation node of Precursor Ions Quantifier through the Proteome Discoverer v2.3 (Thermo Fisher Scientific). For the quantification of phosphoproteomic data, the intensities of phosphopeptides were extracted with initial

precursor mass tolerance set at 10 ppm, minimum number of isotope peaks as 2, maximum ΔRT of isotope pattern multiplets – 0.2 min, PSM confidence FDR of 0.01, with hypothesis test of ANOVA, maximum RT shift of 5 min, pairwise ratio-based ratio calculation, and 100 as the maximum allowed fold change. For calculations of fold-change between the groups of proteins, total phosphoprotein abundance values were added together, and the ratios of these sums were used to compare proteins within different samples.

Quantitative PCR

Total RNA was isolated from midbrain, striatum, and cortex of 1 month-old animals (n=6 animals per group, Lrrk2 WT and Lrrk2 KO) using Animal Tissue RNA Purification Kit (Norgen), according to manufacturer's instruction. After extraction, RNA concentration was quantified with NanoDrop 2000C spectrophotometer (Thermo Fisher Scientific). After DNAse treatment (Thermo Fisher Scientific, according to manufacturer's protocol), complementary DNA (cDNA) was generated using qRT SuperMix (Bimake). The cDNAs were used for quantitative PCR (qPCR) exploiting iTaq Universal SYBR® Green Supermix and CFX96 RealTime System (BioRad) for 40 cycles. All samples were triplicated, and transcripts levels normalized for RPL27 relative abundance (housekeeping gene). Data shown were produced using Bio-Rad CFX Manager software and analyzed according to ddCt algorithm. Primers (5'-3') used are: *Bdnf* FW: GGCTGACACTTTTGAGCACGTC and *Bdnf* REV: CTCCAAAGGCACTTGACTGCTG; *TrkB* FW: TGAGGAGGACACAGGATGTTGA and *Trkb* REV: TTCCAGTGCAAGCCAGTATCTG; *Shank3* FW: ACCTTGAGTCTGTAGATGTGGAAG and *Shank3* REV: GCTTGTGTCCAACCTTCACGAC; *Psd95* FW: GGTGACGACCCATCCATCTTTATC and *Psd95* REV: CGGACATCCACTTCATTGACAAAC; housekeeping *Rpl27* FW AAGCCGTCATCGTGAAGAACA and *Rpl27* REV: CTTGATCTTGGATCGCTTGGC.

Staining on brain tissues and mammalian cells

Immunocytochemistry and confocal microscopy

Mouse primary cortical neurons derived from Lrrk2 WT C57BL/6 and KO pups (P0) were fixed using 4% paraformaldehyde (PFA, Sigma-Aldrich) in PBS pH 7.4 for 20 minutes at room temperature and, after three washes in PBS, they were subjected to staining protocol. Cells were firstly permeabilized with PBS-0.3% Triton-X for 5 minutes and then saturated in blocking buffer [1% Bovine serum Albumin (BSA) Fraction V, 0.1% Triton-X, 50mM Glycine, 2% goat serum in PBS] for 1 hour at room temperature in agitation. The primary and secondary antibodies incubation steps were carried out in working solution (20% blocking buffer in PBS) for 1 hour at room temperature. Both of these two passages were followed by three washes in working solution. Nuclei staining was performed in Hoechst 33258 (Invitrogen, 1:10000 dilution in PBS) for 5 minutes and followed by three rinses in PBS. After been cleaning in distilled water, coverslips were mounted on microscope slides with Mowiol mounting medium. Immunofluorescence z-stack images were obtained on Zeiss LSM700 laser scanning confocal microscope exploiting a 63X oil immersion objective.

The antibodies used for immunocytochemistry were the following: mouse α-PSD95 (ab2723, Abcam, 1:200), rabbit α-MAP2 (sc-20172, Santa Cruz, 1:200); mouse α-drebrin (MA1-20377, Thermo-Fisher, 1:400); goat anti-mouse-Alexa Fluor 568 (A11004, Invitrogen), goat anti-mouse-Alexa Fluor (A11004, Invitrogen), goat anti-rabbit-Alexa Fluor 488 (A11034, Invitrogen), rabbit-Alexa Fluor 568 (A11036, Invitrogen), goat anti-rabbit-Alexa Fluor 405.

Golgi-Cox staining

Animals were terminally anesthetized with xylazine (Rompun®) and ketamine (Zoletil®) cocktail and transcardially perfused with 0.9% saline. Brains were dissected, washed with distilled water and cut into two halves to allow better impregnation. One half was put into Golgi-Cox solution [Potassium dichromate, Mercuric chloride, Potassium chromate prepared according to (Zaqout & Kaindl, 2016)] and stored in the dark at room temperature. After three days, the Golgi-Cox solution was refreshed. The tissues were kept at room temperature in the dark for 14 days and then transferred into a 30% sucrose solution in PBS to avoid the cracking of the slices during the cutting. The brains were embedded in 1.5% agarose low melting point (Promega) and then mounted onto a vibratome stage with glue. The vibratome reservoir was filled with 30% sucrose solution in PBS. Slices of 100 µm in thickness were obtained as this is optimal for dendritic spines studies. While cutting, sections were collected with a thick brush and transferred onto SuperFrost Ultra Plus Adhesion Slides (Thermo Scientific). As soon as all sections have been loaded on slides, the sucrose solution in excess around the sections was cleaned off with absorbent paper. The sections were then blotted by pressing an absorbent paper moistened with sucrose solution onto the slides and dried for 7-10 minutes. The samples were then subjected to colour development procedure consisting in the following passage: 1. two 5-minutes washes in distilled H2O to remove trace of impregnation solution; 2. 5-minutes dehydration step in 50% ethanol; 3. 10-minutes incubation step in 20% ammonium hydroxide; 4. 5-minutes wash in distilled H_2O; 5. 8-minutes incubation step in 5% sodium thiosulfate at room temperature in the dark; 6. two additional 1-minute rinses in distilled H_2O; 7. incubation in ascending grades of ethanol (70%, 95% and 100%) in order to dehydrate the tissue (6 minutes each). After two final 6-minutes incubations with xylene, the slides were covered applying coverslips and Eukitt® mounting medium. Images were acquired with Zeiss LSM700 laser scanning confocal microscope using 100X/1,40 Oil DIC M27 immersion objective with phase contrast acquisition mode.

Statistical analysis

Statistical analyses and plotting were performed with GraphPad-Prism9. Unpaired, two-tailed t-test was used for experiments comparing two groups; one-way ANOVA was used for experiments comparing three or more groups; two-way ANOVA was used when multiple groups and two factors (i.e. genotype and treatment) were to be compared. Šídák's multiple comparisons test was used when determining statistical significance for comparisons between all groups. Statistical significance was calculated among the mean values derived

from the measurements obtained from each individual and the measurements from each individual are presented as smaller dots in the graphs to show variability across individuals.

Acknowledgments

This work was supported by the University of Padova [STARS Grants, LRRKing-Role of the Parkinson's disease kinase LRRK2 in shaping neurites and synapses, EG), the Michael J. Fox Foundation for Parkinson's Research-LRRK2 challenge (EG and LP), and NIH R01 NS097901 (LP).

Author contributions

GT performed the majority of the experiments and analyzed the data; CC performed phosphoproteomics experiments; GF and IB performed AP-MS experiments; MS performed qPCR analysis; NP, LC, GP, GA and LP helped with data analysis and interpretation; AM and FO helped with primary culture protocols and generated preliminary data; CL analyzed MS data; LP designed the phosphoproteomic experiments; EG conceived the study; GT and EG wrote the paper with inputs from all authors.

Figure legends

Figure 1. LRRK2 phosphorylation at ser935 rapidly and transiently increases upon BDNF stimulation in primary mouse cortical neurons and differentiated SH-SY5Y cells.

(a) Schematic representation of the experimental setting of (b).

(b) Phospho-Ser935 and total Lrrk2 protein levels of primary cortical neurons at DIV14 treated with 100 ng/mL BDNF for 0, 5, 30, 60 180 mins. MLi-2 was used at 500 nM for 90 mins to inhibit Lrrk2 kinase activity.

(c) Quantification of n=6 independent experiments of (b).

(d) Schematic representation of the experimental setting of (f) and (g).

(e) TrkB protein levels in undifferentiated or retinoic acid-differentiated SH-SY5Y cells

(f) Phospho Thr202/185 ERK1/2, total ERK1/2, phospho Ser473 AKT, total AKT protein levels of retinoic acid-differentiated SH-SY5Y cells stimulated with 100 ng/mL BDNF for 0, 5, 30, 60 mins.

(g) Phospho-Ser935 and total Lrrk2 protein levels of retinoic acid-differentiated SH-SY5Y cells stimulated with 100 ng/mL BDNF for 0, 5, 30, 60 mins. MLi-2 was used at 500 nM for 90 mins to inhibit Lrrk2 kinase activity.

(h) Quantification of (g) (n=4 independent experiments).

Figure 2. BDNF promotes LRRK2 interaction with post-synaptic actin cytoskeleton components.

(a) Volcano plot of GFP-LRRK2 versus GFP enriched interactors from differentiated SH-SY5Y cells (n=6 replicates: n=3 independent experiments each with 2 technical replicates). Interactors that were considered for SynGO analysis have adjusted p-value < 0.05 and fold change > 2. Red dots represent SynGO terms (only for a subgroup the gene name is reported).

(b) Donut charts with % of SynGO genes among the total LRRK2 interactors (left) and with % of presynaptic and postsynaptic proteins among SynGO genes. SynGO-CC terms visualized with a sunburst plot showing significant categories (below).

(c) Volcano plot of GFP-LRRK2 +/-BDNF enriched interactors from differentiated SH-SY5Y cells (n=6 replicates: n=3 independent experiments each with 2 technical replicates). Interactors selected for pathway enrichment analysis fall into two categories: (i) adjusted p value < 0.05 and fold change > 1 or (ii) fold change > 2. Proteins with increased interaction upon BDNF stimulation are blue-labeled, proteins with decreased interaction are orange-labeled. Donut chart showing the number of SynGO annotated genes versus non synaptic proteins in BDNF-up versus BDNF-down interactors (top right).

(d) g-profiler pathway enrichment analysis showing the top enriched categories of BDNF-increased interactors (top, blue bar graph) versus BDNF-decreased interactors (bottom, orange bar graph).

(e) Protein-Protein Interaction Networks Functional Enrichment Analysis of SynGo BDNF-increased interactors (left, 8 out of 10 hits included in the network) and of SynGo BDNF-decreased interactors (right, 14 out of 21 hits included in the network).
(f) Validation of increased drebrin:LRRK2 interaction upon BDNF treatment (15 mins). Samples are the same analyzed in the three rounds of MS (a).
(g) Quantification of (f).
(h) Confocal immunofluorescence of DIV14 primary neurons co-stained with MAP2 (neuronal marker), PSD95 (postsynaptic marker) and drebrin. Scale bar: 100 µm; magnifications scale bar: 10 µm.

Figure 3. BDNF-induced spinogenesis is impaired in *Lrrk2* knockout neurons.
(a) Overview of the experimental workflow to induce spine formation/maturation.
(b) Representative confocal images of primary cortical neurons stimulated with 100 ng/ml of BDNF or vehicle control for 24 hours. GFP has been transfected at DIV4 to fill the neuroplasm and visualize individual dendrites, MAP2 is a neuronal marker and PSD95 is a marker of mature spines.
(c) Quantification of the number of PSD-positive puncta per unit of length (100 µm). Dots represents individual segments (n≅20 neurites from n=5-6 neurons per replicate) and colors define neuronal cultures prepared in different days from pulled pups (n≅8 pups per culture per genotype, n=3 independent cultures). Two-way ANOVA with Šídák's multiple comparisons test: interaction P=0.0038, F (1, 191) = 8.584; genotype: p=0.5833, F (1, 191) = 0.3020; treatment: p=0.0126, F (1, 191) = 6.346; vehicle vs BDNF (WT) p=0.0005; vehicle vs BDNF (KO) p=0.9440.
(d) DIV14 primary cortical neurons from WT vs KO mice stimulated with BDNF at different time points (0, 5, 15, 30, 60 mins) in the presence or absence of LRRK2 inhibitor MLi-2 (90 min, 500 nM). To compare BDNF-induced signaling in WT vs KO neurons, phosphorylated Akt (S473) and Erk1/2 (T185/T202) were evaluated. Phosphorylated LRRK2 was assessed with pS935 antibodies.
(e) Quantification of phosphorylated proteins show from n=9 independent cultures. Two-way ANOVA with Šídák's multiple comparisons test. Phospho-Akt: interaction P=0.1186, F (3, 63) = 2.031; genotype: p=0.0037, F (1, 63) = 9.101; time: p=0.0342, F (3, 63) = 3.069; multiple comparisons test p=0.0048 WT vs KO 5 mins treatment. Phospho-Erk1: interaction P=0.3256, F (3, 64) = 1.177; genotype: p=0.0201, F (1, 64) = 5.680; time: P<0.0001, F (3, 64) = 10.04; multiple comparisons test p= 0.0478 WT vs KO 30 mins treatment. Phospho-Erk2: interaction P=0.8524, F (3, 62) = 0.2622; genotype: P=0.7528, F (1, 62) = 0.1001; time: F (3, 62) = 7.428.

Figure 4. Striatal spine maturation is delayed in *Lrrk2* knockout mice.
(a) Overview of experimental design.

(b) Representative images of neurite segments from Golgi-Cox stained neurons of dorsal striatum. Scale bar: 3 µm.
(c) Quantification of average spine number (top), width (middle) and length (bottom) of n=3 animals per group (same segments analyzed in b). Statistical significance was determined by two-way ANOVA with Šídák's multiple comparisons test. **Number of protrusions**: interaction P=0.3820, F (2, 12) = 1.044; age: p<0.0001, F (2, 12) = 27.12; genotype: p=0.0840, F (1, 12) = 3.550; WT vs. KO (1 month) p=0.2013; WT vs. KO (4 months) p=0.5080; WT vs. KO (18 months) p>0.9999. **Width:** interaction P=0.0815, F (2, 12) = 3.112; age: p=0.0004, F (2, 12) = 16.14; genotype: p=0.0007, F (1, 12) = 20.77; WT vs. KO (1 month) p=0.0017; WT vs. KO (4 months) p=0.4602; WT vs. KO (18 months) p=0.2489. **Length:** interaction P=0.0345, F (2, 12) = 4.514; age: p=0.0203, F (2, 12) = 5.488; genotype: p=0.0006, F (1, 12) = 21.53; WT vs. KO (1 month) p=0.0008; WT vs. KO (4 months) p=0.2875; WT vs. KO (18 months) p=0.5948.
(d) Morphological classification of protrusions into four classes (filopodia, thin, mushroom, branched) and quantified as % of the total number. Each dot represents one segment ($n \geq 20$ segments analyzed per animal; genotype: wild-type vs. *Lrrk2* KO; age: 1, 4, 18 month-old; n=3 mice per group) and error bars represent the mean ± SD of n=3 mice (color coded). Statistical significance was determined by two-way ANOVA with Šídák's multiple comparisons test on mean values. **One-month**: interaction: p=0.0017, F (3, 16) = 8.018; genotype: p=0.5731, F (1, 16) = 0.3309; class of protrusion: p<0.0001, F (3, 16) = 158.4; filopodia WT vs. KO p=0.0201; thin WT vs. KO p=0.0102; mushroom WT vs. KO p=0.9585; branched WT vs. KO p=0.8726. **Four-months**: interaction: p=0.3178, F (3, 16) = 1.271; genotype: p=0.7300, F (1, 16) = 0.1233; class of protrusion: p<0.0001, F (3, 16) = 438.9; filopodia WT vs. KO p=0.8478; thin WT vs. KO p=0.4921; mushroom WT vs. KO p=0.8882; branched WT vs. KO p=0.9858. **Eighteen-months**: interaction: p=0.3237, F (3, 16) = 1.253; genotype: p=0.6880, F (1, 16) = 0.1672; class of protrusion: p<0.0001, F (3, 16) = 69.67; filopodia WT vs. KO p=0.9756; thin WT vs. KO p=0.6413; mushroom WT vs. KO p>0.9999; branched WT vs. KO p=0.5290.
(e) Representative transmission electron microscopy (TEM) micrographs of striatal synapses from 1-month and 18-month old WT vs KO mouse brain slices (n=3-4 mice per genotype). Scale bar: 200 nm.
(f) Quantification of post-synaptic density (PSD) length. Graphs show the length of individual synapses (grey dots) and the average PSD length per animal (colored dots). Statistical significance has been calculated with Student's t-test: 1 month-old mice (n=4 mice, 95 synapses WT, 118 synapses KO, p=0.0003); 18-month old mice (n=3 mice, 108 synapses WT, 119 synapses KO, p=0.8502).
(g) Quantitative PCR of *Bdnf, TrkB, Psd95* and *Shank3* mRNA expression in striatum, cortex and midbrain form n=6 *Lrrk2* WT and n=6 *Lrrk2* KO one-month old mice. Statistical significance has been calculated with Student's t-test.

Figure 5. Phosphoproteome of Lrrk2^{G2019S} synaptosomes is enriched in postsynaptic structure organization SynGO terms.

(a) Overview of experimental design.
(b) Volcano plot of 2957 differentially phosphopeptides common between WT and Lrrk2^{G2019S} striatal synaptosomes (labeled with gene name) isolated from Lrrk2 WT and Lrrk2^{G2019S} KI mice. Common genes between this analysis and the AP-MS analysis are orange labelled for peptides with decreased phosphorylation and blue labelled for peptides with increased phosphorylation.
(c) Sunburst plot showing enriched SynGO biological processes (BP) categories (267 proteins, at least one significant peptide, $p < 0.05$ and fold change > 0.5).
(d) Sunburst plot showing enriched SynGO cellular component (CC) categories (267 proteins, at least one significant peptide, $p < 0.05$ and fold change > 0.5).

Supplementary figure 1. BDNF increase LRRK2 Ser935 phosphorylation in differentiated SH-SY5Y cells stably overexpressing GFP-LRRK2.
Western blot analysis of differentiated SH-SY5Y cells stably overexpressing GFP-LRRK2 treated with 100 ng/ml BDNF for 5 mins or with 0.5 µM MLi-2 for 90 mins. N=3 technical replicates.

Supplementary figure 2. Spine number and morphology analysis.
(a) Representative images of Golgi-Cox impregnated dorsal striatal slices of 3 month-old WT mouse brains at different magnifications. Scale bar: 50 µm; Magnifications scale bar: 5 µm.
(b) Spine categories defined by shape and dimension analyzed in this study. The bottom panel are representative images of the four spine categories.

Figure 1

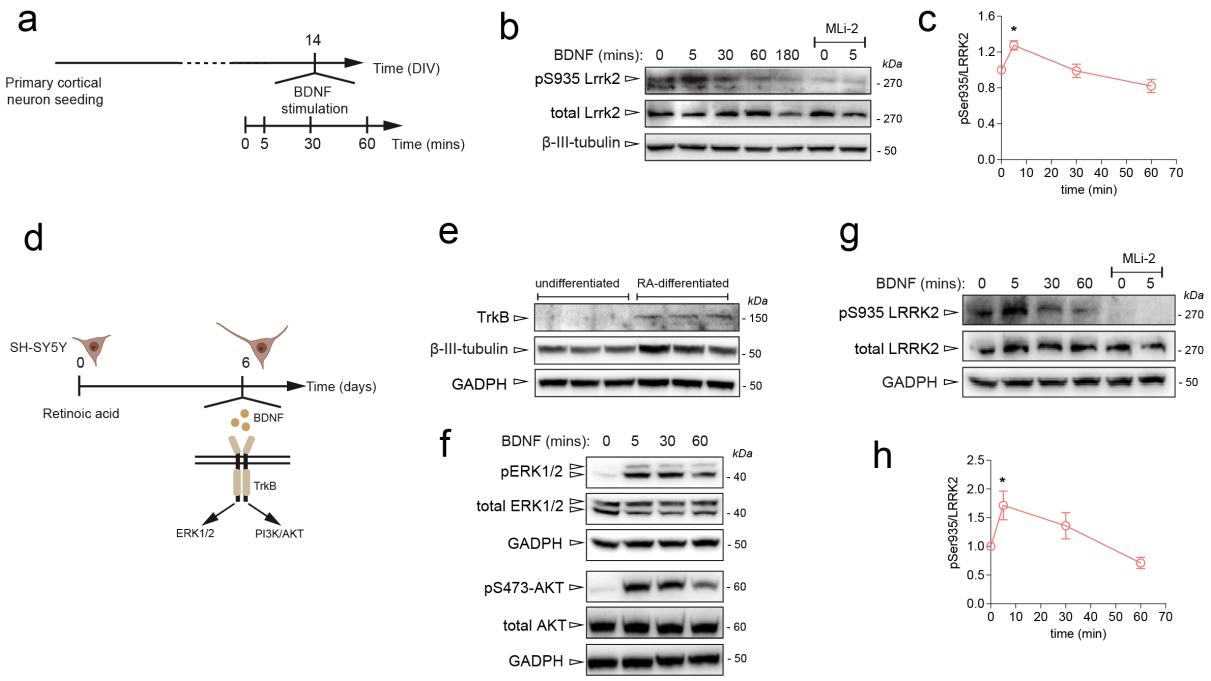
a
14
Time (DIV)
Primary cortical neuron seeding
BDNF stimulation
0 5 30 60 Time (mins)
b
MLi-2
BDNF (mins): 0 5 30 60 180 0 5
kDa
pS935 Lrrk2
total Lrrk2
β-III-tubulin
- 270
- 270
- 50
c
pSer935/LRRK2
time (min)
d
SH-SY5Y
0
6
Time (days)
Retinoic acid
BDNF
TrkB
ERK1/2
PI3K/AKT
e
undifferentiated
RA-differentiated
kDa
TrkB
β-III-tubulin
GADPH
- 150
- 50
- 50
f
BDNF (mins): 0 5 30 60
kDa
pERK1/2
total ERK1/2
GADPH
pS473-AKT
total AKT
GADPH
- 40
- 40
- 50
- 60
- 60
- 50
g
MLi-2
BDNF (mins): 0 5 30 60 0 5
kDa
pS935 LRRK2
total LRRK2
GADPH
- 270
- 270
- 50
h
pSer935/LRRK2
time (min)

Figure 2

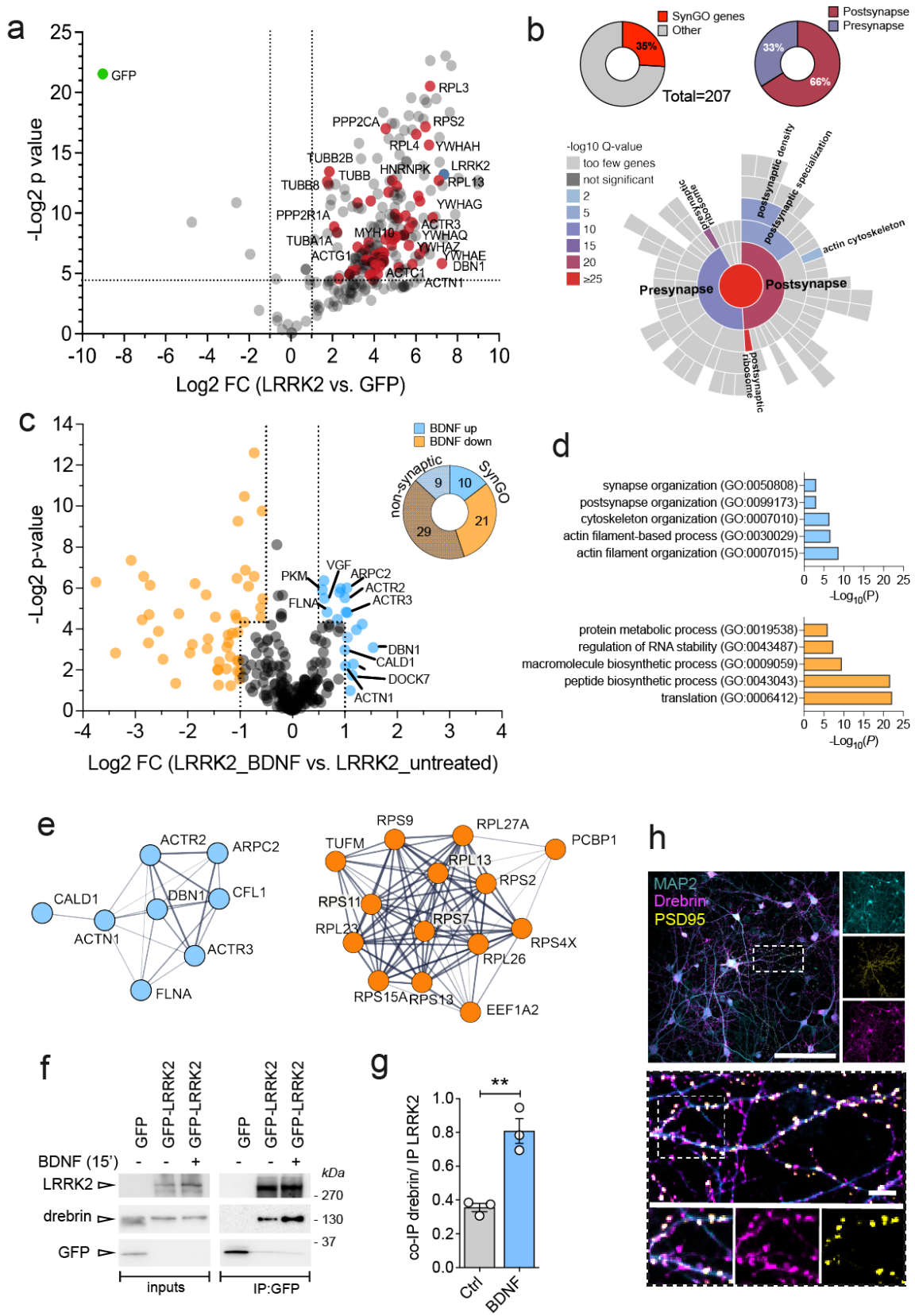
a
GFP
-Log2 p value
Log2 FC (LRRK2 vs. GFP)
RPL3
PPP2CA
RPS2
RPL4
YWHAH
TUBB2B
TUBB
HNRNPK
LRRK2
TUBB8
RPL13
YWHAG
PPP2R1A
ACTR3
MYH10
YWHAQ
TUBA1A
YWHAZ
ACTG1
YWHAE
DBN1
ACTC1
ACTN1
b
SynGO genes
Other
35%
Total=207
Postsynapse
Presynapse
33%
66%
-log10 Q-value
too few genes
not significant
2
5
10
15
20
≥25
postsynaptic density
postsynaptic specialization
presynaptic ribosome
actin cytoskeleton
Presynapse
Postsynapse
postsynaptic ribosome
c
BDNF up
BDNF down
non-synaptic
SynGO
9
10
29
21
-Log2 p-value
Log2 FC (LRRK2_BDNF vs. LRRK2_untreated)
PKM
VGF
ARPC2
ACTR2
ACTR3
FLNA
DBN1
CALD1
DOCK7
ACTN1
d
synapse organization (GO:0050808)
postsynapse organization (GO:0099173)
cytoskeleton organization (GO:0007010)
actin filament-based process (GO:0030029)
actin filament organization (GO:0007015)
-Log10(P)
protein metabolic process (GO:0019538)
regulation of RNA stability (GO:0043487)
macromolecule biosynthetic process (GO:0009059)
peptide biosynthetic process (GO:0043043)
translation (GO:0006412)
-Log10(P)
e
ACTR2
ARPC2
CALD1
DBN1
CFL1
ACTN1
ACTR3
FLNA
RPS9
RPL27A
PCBP1
TUFM
RPL13
RPS2
RPS11
RPS7
RPL23
RPS4X
RPL26
RPS15A
RPS13
EEF1A2
h
MAP2
Drebrin
PSD95
f
GFP
GFP-LRRK2
GFP-LRRK2
GFP
GFP-LRRK2
GFP-LRRK2
BDNF (15')
-
-
+
-
-
+
kDa
LRRK2
drebrin
GFP
270
130
37
inputs
IP:GFP
g
**
co-IP drebrin/ IP LRRK2
Ctrl
BDNF

Figure 3

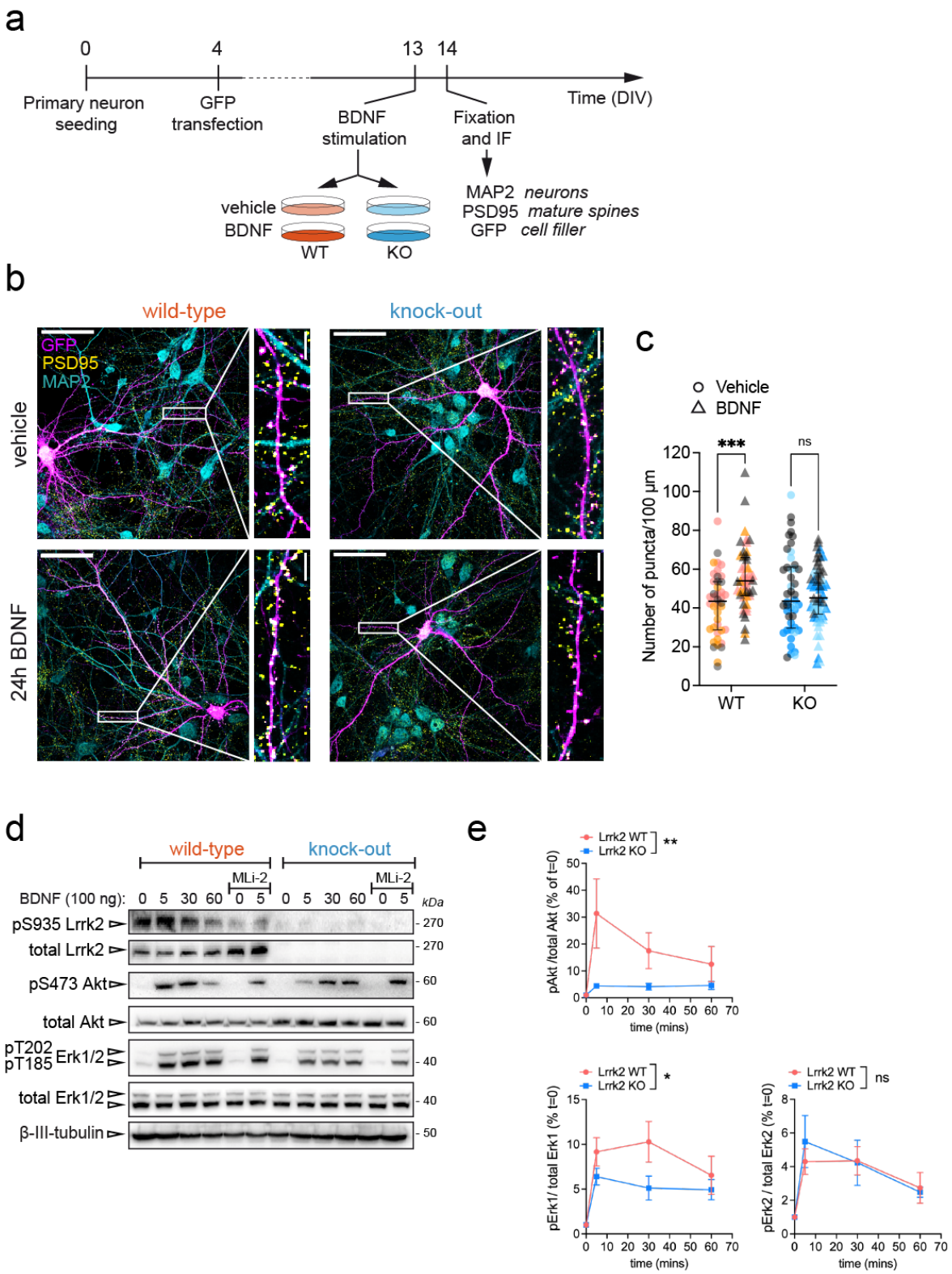
a
0
4
13
14
Primary neuron seeding
GFP transfection
BDNF stimulation
Fixation and IF
Time (DIV)
vehicle
BDNF
WT
KO
MAP2 neurons
PSD95 mature spines
GFP cell filler
b
wild-type
knock-out
GFP
PSD95
MAP2
vehicle
24h BDNF
c
Vehicle
BDNF
***
ns
Number of puncta/100 µm
WT
KO
d
wild-type
knock-out
MLi-2
BDNF (100 ng): 0 5 30 60 0 5 0 5 30 60 0 5
kDa
pS935 Lrrk2
total Lrrk2
pS473 Akt
total Akt
pT202 pT185 Erk1/2
total Erk1/2
β-III-tubulin
270
270
60
60
40
40
50
e
Lrrk2 WT
Lrrk2 KO
**
pAkt /total Akt (% of t=0)
time (mins)
*
pErk1/ total Erk1 (% t=0)
ns
pErk2 / total Erk2 (% t=0)

Figure 4

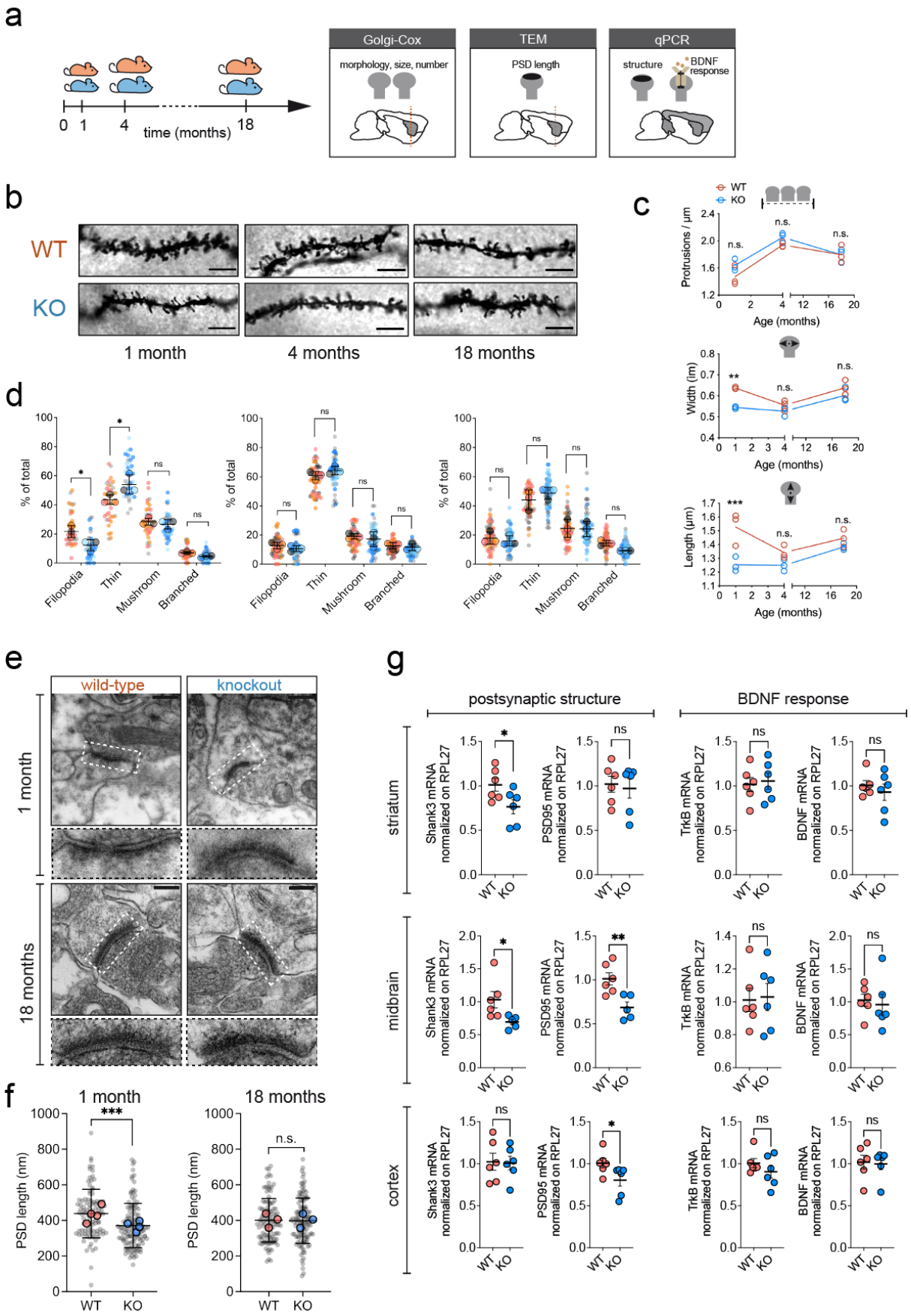
a
0 1 4 18
time (months)
Golgi-Cox
morphology, size, number
TEM
PSD length
qPCR
structure
BDNF response
b
WT
KO
1 month
4 months
18 months
c
WT
KO
Protrusions / µm
Age (months)
Width (µm)
Length (µm)
d
% of total
Filopodia
Thin
Mushroom
Branched
e
wild-type
knockout
1 month
18 months
f
1 month
18 months
PSD length (nm)
WT
KO
g
postsynaptic structure
BDNF response
striatum
midbrain
cortex
Shank3 mRNA normalized on RPL27
PSD95 mRNA normalized on RPL27
TrkB mRNA normalized on RPL27
BDNF mRNA normalized on RPL27

Figure 5

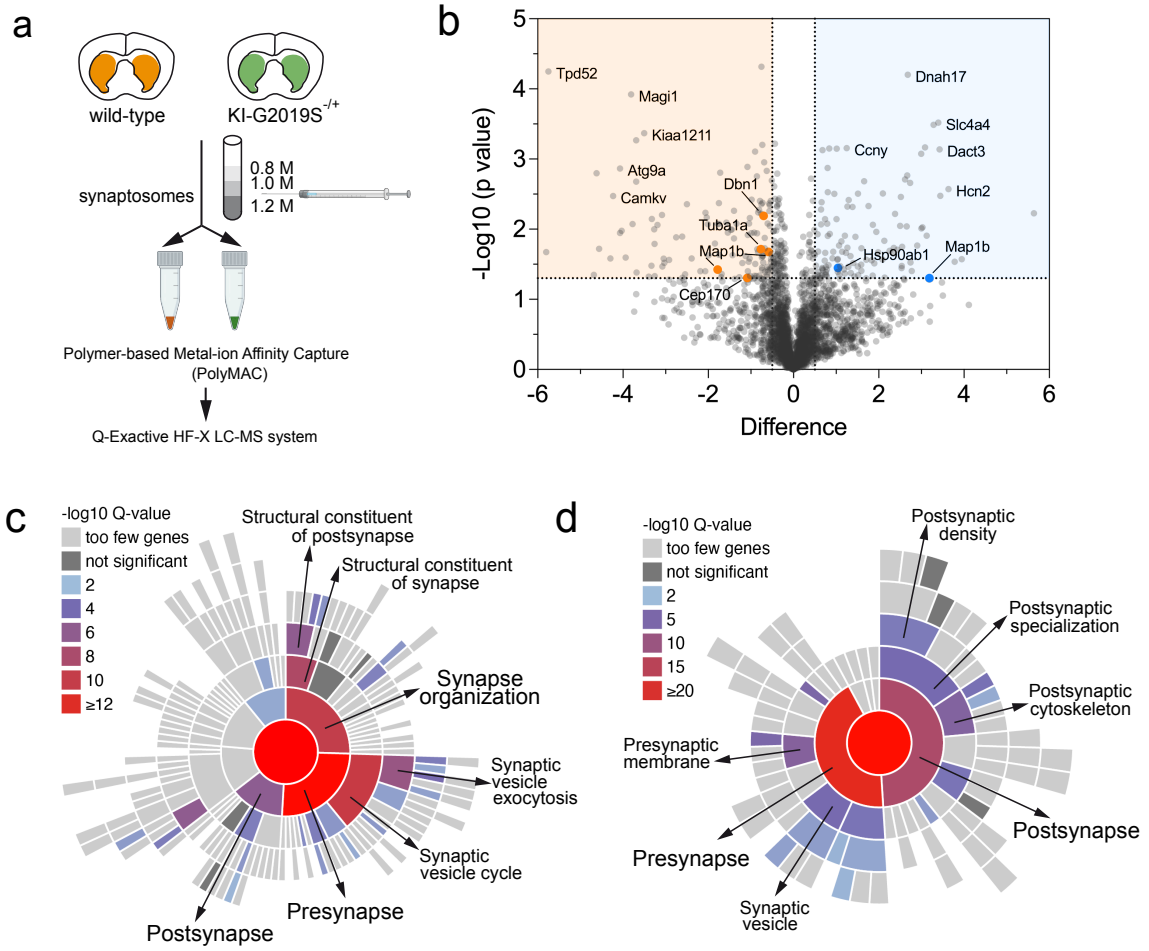
a
wild-type
KI-G2019S-/+
synaptosomes
0.8 M
1.0 M
1.2 M
Polymer-based Metal-ion Affinity Capture
(PolyMAC)
Q-Exactive HF-X LC-MS system
b
-Log10 (p value)
Difference
Tpd52
Magi1
Kiaa1211
Atg9a
Camkv
Dbn1
Tuba1a
Map1b
Cep170
Dnah17
Slc4a4
Ccny
Dact3
Hcn2
Hsp90ab1
Map1b
c
-log10 Q-value
too few genes
not significant
2
4
6
8
10
≥12
Structural constituent of postsynapse
Structural constituent of synapse
Synapse organization
Synaptic vesicle exocytosis
Synaptic vesicle cycle
Presynapse
Postsynapse
d
-log10 Q-value
too few genes
not significant
2
5
10
15
≥20
Postsynaptic density
Postsynaptic specialization
Postsynaptic cytoskeleton
Presynaptic membrane
Postsynapse
Presynapse
Synaptic vesicle

Supplementary figure 1

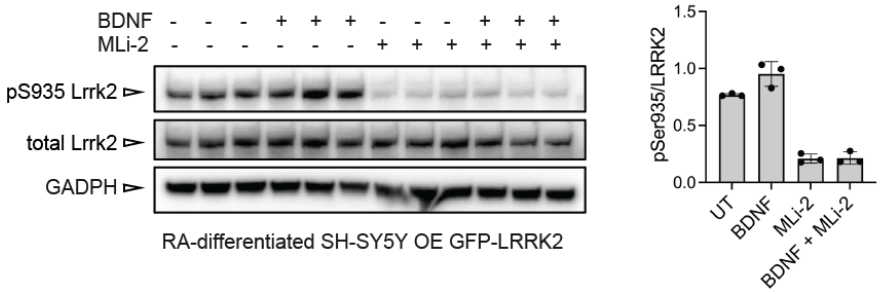

Supplementary figure 2

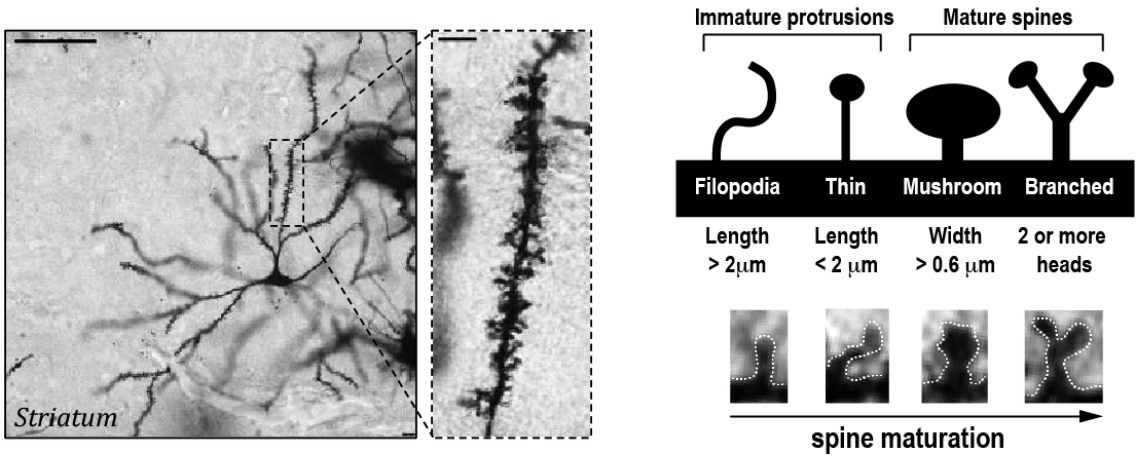

References

1. Harris, K. M. Structure, development, and plasticity of dendritic spines. *Curr. Opin. Neurobiol.* **9**, 343–348 (1999).
2. Harris, K. M. & Kater, S. B. Dendritic spines: Cellular specializations imparting both stability and flexibility to synaptic function. *Annual Review of Neuroscience* vol. 17 341–371 (1994).
3. Hering, H. & Sheng, M. Dentritic spines: structure, dynamics and regulation. *Nat. Rev. Neurosci.* **2**, 880–888 (2001).
4. Nimchinsky, E. A., Sabatini, B. L. & Svoboda, K. Structure and function of dendritic spines. *Annual Review of Physiology* vol. 64 313–353 (2002).
5. Harris, K. M., Jensen, F. E. & Tsao, B. Three-dimensional structure of dendritic spines and synapses in rat hippocampus (CA 1) at postnatal day 15 and adult ages: Implications for the maturation of synaptic physiology and long-term potentiation. *J. Neurosci.* **12**, 2685–2705 (1992).
6. Peters, A. & Kaiserman-Abramof, I. R. The small pyramidal neuron of the rat cerebral cortex. The perikaryon, dendrites and spines. *Am. J. Anat.* **127**, 321–355 (1970).
7. Lendvai, B., Stern, E. A., Chen, B. & Svoboda, K. Experience-dependent plasticity of dendritic spines in the developing rat barrel cortex in vivo. *Nat. 2000 4046780* **404**, 876–881 (2000).
8. Matus, A. Actin-based plasticity in dendritic spines. *Science (80-.).* **290**, 754–758 (2000).
9. Hotulainen, P. & Hoogenraad, C. C. Actin in dendritic spines: Connecting dynamics to function. *Journal of Cell Biology* vol. 189 619–629 (2010).
10. Fiala, J. C., Spacek, J. & Harris, K. M. Dendritic spine pathology: Cause or consequence of neurological disorders? *Brain Research Reviews* vol. 39 29–54 (2002).
11. Hong, S. *et al.* Complement and microglia mediate early synapse loss in Alzheimer mouse models. *Science (80-.).* **352**, 712–716 (2016).
12. Milnerwood, A. J. & Raymond, L. A. Early synaptic pathophysiology in neurodegeneration: Insights from Huntington's disease. *Trends in Neurosciences* vol. 33 513–523 (2010).
13. Picconi, B., Piccoli, G. & Calabresi, P. Synaptic dysfunction in Parkinson's disease. *Adv. Exp. Med. Biol.* **970**, 553–572 (2012).
14. Soukup, S., Vanhauwaert, R. & Verstreken, P. Parkinson's disease: convergence on synaptic homeostasis. *EMBO J.* **37**, (2018).
15. Kordower, J. H. *et al.* Disease duration and the integrity of the nigrostriatal system in Parkinson's disease. *Brain* **136**, 2419–2431 (2013).
16. Bellucci, A., Antonini, A., Pizzi, M. & Spano, P. F. The end is the beginning: Parkinson's disease in the light of brain imaging. *Front. Aging Neurosci.* **9**, (2017).
17. Chidambaram, S. B. *et al.* Dendritic spines: Revisiting the physiological role. *Progress in Neuro-Psychopharmacology and Biological Psychiatry* vol. 92 161–193 (2019).
18. González-Rodríguez, P. *et al.* Disruption of mitochondrial complex I induces progressive parkinsonism. *Nature* **599**, 650–656 (2021).
19. Cookson, M. R. LRRK2 Pathways Leading to Neurodegeneration. *Current Neurology and Neuroscience Reports* vol. 15 (2015).
20. Greggio, E. & Cookson, M. R. Leucine-rich repeat kinase 2 mutations and Parkinson's disease: Three questions. *ASN Neuro* vol. 1 13–24 (2009).

21. Marchand, A., Drouyer, M., Sarchione, A., Chartier-Harlin, M. C. & Taymans, J. M. LRRK2 Phosphorylation, More Than an Epiphenomenon. *Frontiers in Neuroscience* vol. 14 (2020).
22. Wallings, R., Manzoni, C. & Bandopadhyay, R. Cellular processes associated with LRRK2 function and dysfunction. *FEBS Journal* vol. 282 2806–2826 (2015).
23. Civiero, L., Cogo, S., Biosa, A. & Greggio, E. The role of LRRK2 in cytoskeletal dynamics. *Biochemical Society Transactions* vol. 46 1653–1663 (2018).
24. Iannotta, L. & Greggio, E. LRRK2 signaling in neurodegeneration: two decades of progress. *Essays Biochem.* **65**, 859–872 (2021).
25. Nichols, R. J. *et al.* 14-3-3 Binding to LRRK2 is disrupted by multiple Parkinson's disease-associated mutations and regulates cytoplasmic localization. *Biochem. J.* **430**, 393–404 (2010).
26. Pischedda, F. & Piccoli, G. LRRK2 at the pre-synaptic site: A 16-years perspective. *Journal of Neurochemistry* vol. 157 297–311 (2021).
27. Belluzzi, E. *et al.* LRRK2 phosphorylates pre-synaptic N-ethylmaleimide sensitive fusion (NSF) protein enhancing its ATPase activity and SNARE complex disassembling rate. *Mol. Neurodegener.* **11**, (2016).
28. Marte, A. *et al.* Leucine-rich repeat kinase 2 phosphorylation on synapsin I regulates glutamate release at pre-synaptic sites. *J. Neurochem.* **150**, 264–281 (2019).
29. Rassu, M. *et al.* Role of LRRK2 in the regulation of dopamine receptor trafficking. *PLoS One* **12**, (2017).
30. Chen, C. *et al.* Pathway-specific dysregulation of striatal excitatory synapses by LRRK2 mutations. *Elife* **9**, 1–26 (2020).
31. Matikainen-Ankney, B. A. *et al.* Altered development of synapse structure and function in striatum caused by Parkinson's disease-linked LRRK2-G2019S mutation. *J. Neurosci.* **36**, 7128–7141 (2016).
32. Parisiadou, L. *et al.* LRRK2 regulates synaptogenesis and dopamine receptor activation through modulation of PKA activity. *Nat. Neurosci.* **17**, 367–376 (2014).
33. Mandemakers, W., Snellinx, A., O'Neill, M. J. & de Strooper, B. LRRK2 expression is enriched in the striosomal compartment of mouse striatum. *Neurobiol. Dis.* **48**, 582–593 (2012).
34. West, A. B. *et al.* Differential LRRK2 expression in the cortex, striatum, and substantia nigra in transgenic and nontransgenic rodents. *J. Comp. Neurol.* **522**, 2465–2480 (2014).
35. Dzamko, N. *et al.* The IkappaB kinase family phosphorylates the Parkinson's disease kinase LRRK2 at Ser935 and Ser910 during Toll-Like Receptor signaling. *PLoS One* **7**, (2012).
36. Muda, K. *et al.* Parkinson-related LRRK2 mutation R1441C/G/H impairs PKA phosphorylation of LRRK2 and disrupts its interaction with 14-3-3. *Proc. Natl. Acad. Sci. U. S. A.* **111**, (2014).
37. Chia, R. *et al.* Phosphorylation of LRRK2 by casein kinase 1α regulates trans-Golgi clustering via differential interaction with ARHGEF7. *Nat. Commun.* **5**, (2014).
38. Dzamko, N. *et al.* Inhibition of LRRK2 kinase activity leads to dephosphorylation of Ser 910/Ser935, disruption of 14-3-3 binding and altered cytoplasmic localization. *Biochem. J.* **430**, 405–413 (2010).
39. Nazish, I. *et al.* Abrogation of LRRK2 dependent Rab10 phosphorylation with TLR4 activation and alterations in evoked cytokine release in immune cells. *Neurochem. Int.*

147, (2021).
40. Thoenen, H. Neurotrophins and neuronal plasticity. *Science (80-.).* **270**, 593–598 (1995).
41. Baydyuk, M. & Xu, B. BDNF signaling and survival of striatal neurons. *Frontiers in Cellular Neuroscience* vol. 8 (2014).
42. Iannotta, L. *et al.* Divergent Effects of G2019S and R1441C LRRK2 Mutations on LRRK2 and Rab10 Phosphorylations in Mouse Tissues. *Cells* **9**, (2020).
43. Skelton, P. D., Tokars, V. & Parisiadou, L. LRRK2 at Striatal Synapses: Cell-Type Specificity and Mechanistic Insights. *Cells* vol. 11 (2022).
44. Piccoli, G. *et al.* LRRK2 controls synaptic vesicle storage and mobilization within the recycling pool. *J. Neurosci.* **31**, 2225–2237 (2011).
45. Kluss, J. H., Lewis, P. A. & Greggio, E. Leucine-rich repeat kinase 2 (LRRK2): an update on the potential therapeutic target for Parkinson's disease. *Expert Opinion on Therapeutic Targets* vol. 26 537–546 (2022).
46. Encinas, M. *et al.* Sequential treatment of SH-SY5Y cells with retinoic acid and brain-derived neurotrophic factor gives rise to fully differentiated, neurotrophic factor-dependent, human neuron-like cells. *J. Neurochem.* **75**, 991–1003 (2000).
47. Numakawa, T. *et al.* BDNF function and intracellular signaling in neurons. *Histology and Histopathology* vol. 25 237–258 (2010).
48. Manzoni, C., Denny, P., Lovering, R. C. & Lewis, P. A. Computational analysis of the LRRK2 interactome. *PeerJ* **2015**, (2015).
49. Tomkins, J. E. *et al.* Comparative Protein Interaction Network Analysis Identifies Shared and Distinct Functions for the Human ROCO Proteins. *Proteomics* **18**, (2018).
50. Koopmans, F. *et al.* SynGO: An Evidence-Based, Expert-Curated Knowledge Base for the Synapse. *Neuron* **103**, 217-234.e4 (2019).
51. Koganezawa, N., Hanamura, K., Sekino, Y. & Shirao, T. The role of drebrin in dendritic spines. *Molecular and Cellular Neuroscience* vol. 84 85–92 (2017).
52. Kellner, Y. *et al.* The BDNF effects on dendritic spines of mature hippocampal neurons depend on neuronal activity. *Front. Synaptic Neurosci.* **6**, (2014).
53. Zagrebelsky, M. & Korte, M. Form follows function: BDNF and its involvement in sculpting the function and structure of synapses. *Neuropharmacology* vol. 76 628–638 (2014).
54. Lai, K. O. *et al.* TrkB phosphorylation by Cdk5 is required for activity-dependent structural plasticity and spatial memory. *Nat. Neurosci.* **15**, 1506–1515 (2012).
55. Ji, Y., Pang, P. T., Feng, L. & Lu, B. Cyclic AMP controls BDNF-induced TrkB phosphorylation and dendritic spine formation in mature hippocampal neurons. *Nat. Neurosci.* **8**, 164–172 (2005).
56. Koleske, A. J. Molecular mechanisms of dendrite stability. *Nature Reviews Neuroscience* vol. 14 536–550 (2013).
57. Surmeier, D. J., Obeso, J. A. & Halliday, G. M. Selective neuronal vulnerability in Parkinson disease. *Nature Reviews Neuroscience* vol. 18 101–113 (2017).
58. Westerlund, M. *et al.* Developmental regulation of leucine-rich repeat kinase 1 and 2 expression in the brain and other rodent and human organs: Implications for Parkinson's disease. *Neuroscience* **152**, 429–436 (2008).
59. Tong, Y. *et al.* R1441C mutation in LRRK2 impairs dopaminergic neurotransmission in mice. *Proc. Natl. Acad. Sci. U. S. A.* **106**, 14622–14627 (2009).
60. Volta, M. *et al.* Initial elevations in glutamate and dopamine neurotransmission decline

with age, as does exploratory behavior, in LRRK2 G2019S knock-in mice. *Elife* **6**, (2017).
61. Lee, J. H. *et al.* Parkinson's disease-associated LRRK2-G2019S mutant acts through regulation of SERCA activity to control ER stress in astrocytes. *Acta Neuropathol. Commun.* **7**, 68 (2019).
62. Reyniers, L. *et al.* Differential protein protein interactions of LRRK1 and LRRK2 indicate roles in distinct cellular signaling pathways. *J. Neurochem.* **131**, 239–250 (2014).
63. Dächsel, J. C. *et al.* Identification of potential protein interactors of Lrrk2. *Park. Relat. Disord.* **13**, 382–385 (2007).
64. Liu, G. H. *et al.* Progressive degeneration of human neural stem cells caused by pathogenic LRRK2. *Nature* **491**, 603–607 (2012).
65. Ivanov, A., Esclapez, M., Pellegrino, C., Shirao, T. & Ferhat, L. Drebrin A regulates dendritic spine plasticity and synaptic function in mature cultured hippocampal neurons. *J. Cell Sci.* **122**, 524–534 (2009).
66. Tanabe, K. *et al.* Phosphorylation of Drebrin by Cyclin-dependent Kinase 5 and Its role in neuronal migration. *PLoS One* **9**, (2014).
67. Blom, N., Gammeltoft, S. & Brunak, S. Sequence and structure-based prediction of eukaryotic protein phosphorylation sites. *J. Mol. Biol.* **294**, 1351–1362 (1999).
68. Blom, N., Sicheritz-Pontén, T., Gupta, R., Gammeltoft, S. & Brunak, S. Prediction of post-translational glycosylation and phosphorylation of proteins from the amino acid sequence. *Proteomics* vol. 4 1633–1649 (2004).
69. Piccoli, G. *et al.* Leucine-Rich Repeat Kinase 2 Binds to Neuronal Vesicles through Protein Interactions Mediated by Its C-Terminal WD40 Domain. *Mol. Cell. Biol.* **34**, 2147–2161 (2014).
70. Cirnaru, M. D. *et al.* LRRK2 kinase activity regulates synaptic vesicle trafficking and neurotransmitter release through modulation of LRRK2 macro-molecular complex. *Front. Mol. Neurosci.* **7**, (2014).
71. Maas, J. W., Yang, J. & Edwards, R. H. Endogenous leucine-rich repeat kinase 2 slows synaptic vesicle recycling in striatal neurons. *Front. Synaptic Neurosci.* **9**, (2017).
72. Arranz, A. M. *et al.* LRRK2 functions in synaptic vesicle endocytosis through a kinasedependent mechanism. *J. Cell Sci.* **128**, 541–552 (2015).
73. Nguyen, M. & Krainc, D. LRRK2 phosphorylation of auxilin mediates synaptic defects in dopaminergic neurons from patients with Parkinson's disease. *Proc. Natl. Acad. Sci. U. S. A.* **115**, 5576–5581 (2018).
74. Cao, M. *et al.* Parkinson Sac Domain Mutation in Synaptojanin 1 Impairs Clathrin Uncoating at Synapses and Triggers Dystrophic Changes in Dopaminergic Axons. *Neuron* **93**, 882-896.e5 (2017).
75. Soukup, S. F. *et al.* A LRRK2-Dependent EndophilinA Phosphoswitch Is Critical for Macroautophagy at Presynaptic Terminals. *Neuron* **92**, 829–844 (2016).
76. Beccano-Kelly, D. A. *et al.* LRRK2 overexpression alters glutamatergic presynaptic plasticity, striatal dopamine tone, postsynaptic signal transduction, motor activity and memory. *Hum. Mol. Genet.* **24**, 1336–1349 (2015).
77. Hedrick, N. G. *et al.* Rho GTPase complementation underlies BDNF-dependent homo- and heterosynaptic plasticity. *Nature* **538**, 104–108 (2016).
78. Chan, D., Citro, A., Cordy, J. M., Shen, G. C. & Wolozin, B. Rac1 protein rescues neurite retraction caused by G2019s leucine-rich repeat kinase 2 (LRRK2). *J. Biol. Chem.* **286**, 16140–16149 (2011).
79. Feng, M. *et al.* Distinctive roles of Rac1 and Rab29 in LRRK2 mediated membrane

trafficking and neurite outgrowth. *J. Biomed. Res.* **32**, 145–156 (2018).
80. Meixner, A. *et al.* A QUICK screen for Lrrk2 interaction partners - Leucine-rich repeat kinase 2 is involved in actin cytoskeleton dynamics. *Mol. Cell. Proteomics* **10**, (2011).
81. Takahashi, H. *et al.* Drebrin-dependent actin clustering in dendritic filopodia governs synaptic targeting of postsynaptic density-95 and dendritic spine morphogenesis. *J. Neurosci.* **23**, 6586–6595 (2003).
82. Aoki, C. *et al.* Drebrin a knockout eliminates the rapid form of homeostatic synaptic plasticity at excitatory synapses of intact adult cerebral cortex. *J. Comp. Neurol.* **517**, 105–121 (2009).
83. Sekino, Y. *et al.* Activation of N-methyl-d-aspartate receptor induces a shift of drebrin distribution: Disappearance from dendritic spines and appearance in dendritic shafts. *Mol. Cell. Neurosci.* **31**, 493–504 (2006).
84. Spence, E. F., Kanak, D. J., Carlson, B. R. & Soderling, S. H. The Arp2/3 complex is essential for distinct stages of spine synapse maturation, including synapse unsilencing. *J. Neurosci.* **36**, 9696–9709 (2016).
85. Kim, K. S. *et al.* Regulation of myeloid cell phagocytosis by LRRK2 via WAVE2 complex stabilization is altered in Parkinson's disease. *Proc. Natl. Acad. Sci. U. S. A.* **115**, E5164–E5173 (2018).
86. Giaime, E. *et al.* Age-Dependent Dopaminergic Neurodegeneration and Impairment of the Autophagy-Lysosomal Pathway in LRRK-Deficient Mice. *Neuron* **96**, 796-807.e6 (2017).
87. Huang, G. *et al.* Motor Impairments and Dopaminergic Defects Caused by Loss of Leucine-Rich Repeat Kinase Function in Mice. *J. Neurosci.* **42**, 4755–4765 (2022).
88. Biskup, S. *et al.* Dynamic and redundant regulation of LRRK2 and LRRK1 expression. *BMC Neurosci.* **8**, (2007).
89. Cogo, S. *et al.* The Roc domain of LRRK2 as a hub for protein-protein interactions: a focus on PAK6 and its impact on RAB phosphorylation. *Brain Res.* **1778**, (2022).
90. Qualmann, B., Boeckers, T. M., Jeromin, M., Gundelfinger, E. D. & Kessels, M. M. Linkage of the Actin Cytoskeleton to the Postsynaptic Density via Direct Interactions of Abp1 with the ProSAP/Shank Family. *J. Neurosci.* **24**, 2481–2495 (2004).
91. Narita, M., Aoki, K., Takagi, M., Yajima, Y. & Suzuki, T. Implication of brain-derived neurotrophic factor in the release of dopamine and dopamine-related behaviors induced by methamphetamine. *Neuroscience* **119**, 767–775 (2003).
92. Morella, I., Hallum, H. & Brambilla, R. Dopamine D1 and Glutamate Receptors Co-operate With Brain-Derived Neurotrophic Factor (BDNF) and TrkB to Modulate ERK Signaling in Adult Striatal Slices. *Front. Cell. Neurosci.* **14**, (2020).
93. Hyman, C. *et al.* BDNF is a neurotrophic factor for dopaminergic neurons of the substantia nigra. *Nature* **350**, 230–232 (1991).
94. Baquet, Z. C., Bickford, P. C. & Jones, K. R. Brain-derived neurotrophic factor is required for the establishment of the proper number of dopaminergic neurons in the substantia nigra pars compacta. *J. Neurosci.* **25**, 6251–6259 (2005).
95. Rahmani, F. *et al.* Plasma levels of brain-derived neurotrophic factor in patients with Parkinson disease: A systematic review and meta-analysis. *Brain Res.* **1704**, 127–136 (2019).
96. Lin, C. H., Wu, R. M., Tai, C. H., Chen, M. L. & Hu, F. C. Lrrk2 S1647T and BDNF V66M interact with environmental factors to increase risk of Parkinson's disease. *Park. Relat. Disord.* **17**, 84–88 (2011).

97. Liu, J. *et al.* Brain-derived neurotrophic factor (BDNF) genetic polymorphism greatly increases risk of leucine-rich repeat kinase 2 (LRRK2) for Parkinson's disease. *Park. Relat. Disord.* **18**, 140–143 (2012).
98. Siuda, J. *et al.* Cognitive impairment and BDNF serum levels. *Neurol. Neurochir. Pol.* **51**, 24–32 (2017).
99. Ziebell, M. *et al.* Striatal dopamine transporter binding correlates with serum BDNF levels in patients with striatal dopaminergic neurodegeneration. *Neurobiol. Aging* **33**, 428.e1-428.e5 (2012).
100. Tagliaferro, P. & Burke, R. E. Retrograde Axonal Degeneration in Parkinson Disease. *Journal of Parkinson's Disease* vol. 6 1–15 (2016).
101. Aguilan, J. T., Kulej, K. & Sidoli, S. Guide for protein fold change and: P-value calculation for non-experts in proteomics. *Mol. Omi.* **16**, 573–582 (2020).
102. Lazar, C., Gatto, L., Ferro, M., Bruley, C. & Burger, T. Accounting for the Multiple Natures of Missing Values in Label-Free Quantitative Proteomics Data Sets to Compare Imputation Strategies. *J. Proteome Res.* **15**, 1116–1125 (2016).